RESEARCH ARTICLE SUMMARY

NEUROSCIENCE

Synaptic architecture of a memory engram in the mouse hippocampus

Marco Uytiepo†, Yongchuan Zhu†, Eric Bushong, Katherine Chou, Filip Souza Polli, Elise Zhao, Keun-Young Kim, Danielle Luu, Lyanne Chang, Dong Yang, Tsz Ching Ma, Mingi Kim, Yuting Zhang, Grant Walton, Tom Quach, Matthias Haberl, Luca Patapoutian, Arya Shahbazi, Yuxuan Zhang, Elizabeth Beutter, Weiheng Zhang, Brian Dong, Aureliano Khoury, Alton Gu, Elle McCue, Lisa Stowers, Mark Ellisman, Anton Maximov*

INTRODUCTION: The architectures of brain circuits reflect their capacities for information processing, storage, and retrieval. Long-term memories of new experiences are thought to form through mechanisms involving the restructuring of both neuronal wiring and individual synapses. The classic Hebbian theory posits that neurons recruited for discrete learning epochs form stable networks by selectively strengthening connections among themselves. However, the generalizability of this principle is challenged by observations suggesting that the population coding of sensory stimuli is not consistently fixed over time and that neural ensembles engaged during memory acquisition and recall only partially overlap across different brain regions.

RATIONALE: Current insights into the nature and origins of experience-dependent events that shape the physical substrates of memory engrams are largely derived from optical imaging. Despite ongoing technical advancements, light-imaging methods alone remain insufficient for the detailed dissection of complex brain tissues because of their limited resolution and inability to provide unbiased analyses of diverse structural features. Consequently, the intricate organization of circuits that store memory traces remains poorly understood. To address this knowledge gap, we used three-dimensional electron microscopy (3D-EM). By integrating 3D-EM with temporally controlled chemogenetic tagging of behaviorally relevant neurons and artificial intelligence–based tools for image analysis, we aimed to uncover the structural correlates of long-term associative memory in the mouse hippocampus.

RESULTS: We performed nanoscale reconstructions of the hippocampal CA3-CA1 pathway, where projection neurons (PNs) recruited during Pavlovian fear conditioning were irreversibly labeled in a dual *Fos*- and drug-inducible manner using the engineered peroxidase APEX2. PNs with a remote history of activity coinciding with associative learning displayed no strong preference for wiring with one another. Instead, these PNs reorganized their connectivity through atypical multisynaptic boutons (MSBs) without altering the number or spatial distribution of isolated nerve terminals and dendritic spines. CA3 PNs expanded their axonal networks in CA1 by increasing both the relative abundance of MSBs and their structural complexity. This expansion was driven by presynaptic excitation elicited by negative valence stimuli, but not by neutral stimuli, and occurred independently of the coactivation state of postsynaptic partners. MSB-mediated rewiring of ensembles representing initial engrams was accompanied by spatially restricted, input-specific upscaling of individual synapses, remodeling of presynaptic mitochondria, redistribution of the postsynaptic spine apparatus, and enhanced interactions with astrocytes.

CONCLUSION: Our study elucidates the physical hallmarks of long-term memory at cellular and subcellular levels. High-resolution imaging of excitatory circuits and synapses allocated for an engram provides a structural basis for the cellular flexibility of information coding, as previously observed in brain regions critical for various sensory modalities and associative learning. Our findings highlight a mechanism by which projection neurons involved in memory acquisition increase their wiring complexity while maintaining the steady-state arrangements of individual synaptic sites. This mechanism may enhance a network's associative capacity, facilitate ensemble sharing for memory generalization, and/or improve the efficiency of temporal coding. Collectively, our results establish a framework for advancing the understanding of how sensory experience–dependent structural plasticity in brain circuits affects their computational properties. ■

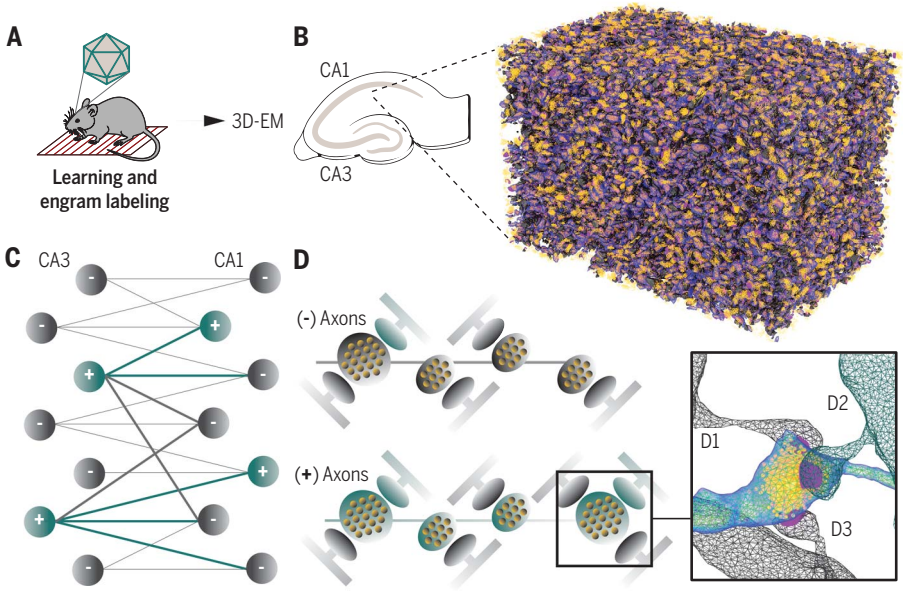

Ultrastructural analysis of the physical substrates of memory engrams in the mouse hippocampus. (**A**) Overview of the experimental design. (**B**) A saturated 3D-EM reconstruction of excitatory synapses in the stratum radiatum of the dorsal area CA1. (**C**) Diagram illustrating the absence of preferential wiring among projection neurons activated during associative learning in areas CA3 and CA1 alongside the expansion of axonal networks of CA3 neurons. (**D**) Diagram depicting the expansion of axonal connectivity in initial engram ensembles through atypical MSBs. A 3D view of an individual MSB connecting to three dendritic branches (D1 to D3) is also shown.

The list of author affiliations is available in the full article online.
***Corresponding author. Email: amaximov@scripps.edu**
†These authors contributed equally to this work.
Cite this article as M. Uytiepo *et al.*, *Science* 387, eado8316 (2025). DOI: 10.1126/science.ado8316

READ THE FULL ARTICLE AT
https://doi.org/10.1126/science.ado8316

RESEARCH ARTICLE

NEUROSCIENCE

Synaptic architecture of a memory engram in the mouse hippocampus

Marco Uytiepo[1,2,3]†, Yongchuan Zhu[1,2]†‡, Eric Bushong[4,5], Katherine Chou[1,2], Filip Souza Polli[1,2]§, Elise Zhao[1,2], Keun-Young Kim[4,5], Danielle Luu[1,2], Lyanne Chang[1,2], Dong Yang[1,2], Tsz Ching Ma[1,2], Mingi Kim[1,2,3], Yuting Zhang[1,2,3], Grant Walton[1,2], Tom Quach[1,2], Matthias Haberl[4,5], Luca Patapoutian[1,2], Arya Shahbazi[1,2], Yuxuan Zhang[1,2], Elizabeth Beutter[1,2], Weiheng Zhang[1,2], Brian Dong[1,2], Aureliano Khoury[1,2], Alton Gu[1,2], Elle McCue[1,2], Lisa Stowers[1,2], Mark Ellisman[4,5], Anton Maximov[1,2]*

Memory engrams are formed through experience-dependent plasticity of neural circuits, but their detailed architectures remain unresolved. Using three-dimensional electron microscopy, we performed nanoscale reconstructions of the hippocampal CA3-CA1 pathway after chemogenetic labeling of cellular ensembles recruited during associative learning. Neurons with a remote history of activity coinciding with memory acquisition showed no strong preference for wiring with each other. Instead, their connectomes expanded through multisynaptic boutons independently of the coactivation state of postsynaptic partners. The rewiring of ensembles representing an initial engram was accompanied by input-specific, spatially restricted upscaling of individual synapses, as well as remodeling of mitochondria, smooth endoplasmic reticulum, and interactions with astrocytes. Our findings elucidate the physical hallmarks of long-term memory and offer a structural basis for the cellular flexibility of information coding.

The acquisition of long-term memories is widely believed to involve structural changes in the brain. This conceptual framework is supported by substantial empirical evidence demonstrating that sensory stimuli regulate neuronal morphologies and connectivity within brain regions essential for associative, spatial, and motor learning (*1*–*4*). However, the intricate architectures of circuits that store memory traces remain poorly understood.

The classic Hebbian theory, encapsulated by the axiom "fire together, wire together," postulates that learning arises from a selective increase in synaptic weights between connected neurons as a result of their simultaneous excitation (*5*). Hebbian mechanisms can manifest through the strengthening of existing synapses and/or the formation of new contacts (*5*–*7*). The neural substrates of memory engrams have been extensively studied using approaches that leverage the immediate early gene *Fos* to trace and manipulate ensembles with transient activity that coincides with Pavlovian learning (*8*). Optogenetic reactivation of these ensembles has been shown to retrieve memories in the absence of external cues, whereas their inhibition disrupts normal retrieval (*2*, *9*–*11*). However, the generalizability of the Hebbian rule is challenged by findings that pools of neurons marked by *Fos* reporters during learning and memory recall only partially overlap in virtually every relevant brain region (*8*, *12*). A similar phenomenon, called representational drift, has been observed through repeated detection of cellular correlates of the same stimulus over time (*13*–*18*).

Theoretically, the "drifts" within circuits representing an engram could reflect at least three nonmutually exclusive scenarios: (i) Ensembles allocated to an initial learning episode may already be part of a broader interconnected network, in which the recruitment of individual neurons is stochastic; (ii) these ensembles may reorganize their physical connectivity, establishing contacts with other neurons after novel experiences; and (iii) the patterns of cellular coding within a preexisting network may shift due to an experience-dependent redistribution of functional weights. To explore these possibilities, we used serial block face-scanning electron microscopy (SBEM), a technique for three-dimensional (3D) nanoscale reconstruction of biological tissues (*19*).

Contemporary 3D-EM methods have been instrumental in unraveling the organization of nervous systems in different species (*20*–*29*). Because of the challenges in reconstructing large tissue volumes, most comprehensive connectomic analyses to date have been conducted on single specimens (*20*, *21*, *24*, *25*, *27*, *29*). Therefore, these studies do not explain how brain wiring is influenced by external environment or internal states. Here, we combined SBEM with chemogenetic tagging of behaviorally relevant neurons and artificial intelligence (AI) algorithms for image segmentation to identify the hallmarks of memory engrams at scales ranging from local connectomes to synaptic subcompartments.

Results

Permanent labeling of hippocampal engrams with APEX2-mGFP

We searched for structural correlates of long-term information storage in the hippocampus of mice subjected to contextual fear conditioning (CFC), a Pavlovian paradigm for acquiring associative memory of an aversive environment in which neutral visual and olfactory cues are paired with unpleasant foot shocks (*2*, *8*). To accommodate the need for sampling 3D images with a nanometer resolution from multiple animals, we focused on the stratum radiatum (sr) of hippocampal area CA1, where dendrites of pyramidal glutamatergic neurons (PNs) are innervated by Schaffer collateral (SchC) axons of PNs residing in the upstream area CA3 (Fig. 1A). The importance of the CA3-CA1 pathway for associative learning and memory has been well established (*12*, *30*). Given that cellular ensembles recruited for each learning epoch are sparse (*2*, *8*, *12*), we devised a workflow for irreversible labeling of transiently activated populations with an engineered peroxidase, APEX2-mGFP (*31*, *32*) (Fig. 1B and fig. S1). This membrane-anchored, EM-compatible marker was introduced with the Cre recombinase-inducible adeno-associated virus (AAVDJ-DIO: APEX2-mGFP) into the hippocampus of knock-in mice that express destabilized Cre (DD-Cre) under the control of the endogenous *Fos* promoter ($Fos^{DD\text{-}Cre}$) (*33*–*35*). *Fos* is an immediate early gene whose transcription is restricted to narrow windows after neuronal excitation (*8*, *36*). Newly synthesized DD-Cre undergoes rapid proteasomal degradation, but this process can be blocked by peripheral delivery of the blood-brain barrier (BBB)–permeable antibiotic trimethoprim (TMP) (*34*, *37*). Because free TMP crosses the BBB within minutes and has fast kinetics of clearance from the brain (*34*), the $Fos^{DD\text{-}Cre}$ allele permits temporally restricted recombination of *LoxP*-flanked DNA sequences in neurons activated by specific stimuli, similar to the tamoxifen-inducible $Fos^{Cre\text{-}ERT2}$ (*33*, *35*, *38*, *39*). All analyses described herein were conducted with young adult heterozygote $Fos^{DD\text{-}Cre}$ mice 1 week after behavioral conditioning (Fig. 1C and fig. S2). This timeline was chosen to investigate the effects of novel experiences that

[1]Department of Neuroscience, The Scripps Research Institute, La Jolla, CA, USA. [2]The Dorris Neuroscience Center, The Scripps Research Institute, La Jolla, CA, USA. [3]The Skaggs Graduate School of Chemical and Biological Sciences, The Scripps Research Institute, La Jolla, CA, USA. [4]National Center for Microscopy and Imaging Research, University of California, San Diego, San Diego, CA, USA. [5]Department of Neurosciences, University of California, San Diego, School of Medicine, La Jolla, CA, USA.
*Corresponding author. Email: amaximov@scripps.edu
†These authors contributed equally to this work.
‡Present address: Mental Health Center, Shanghai Jiao Tong University School of Medicine, Shanghai, China.
§Present address: H. Lundbeck A/S, Copenhagen, Denmark.

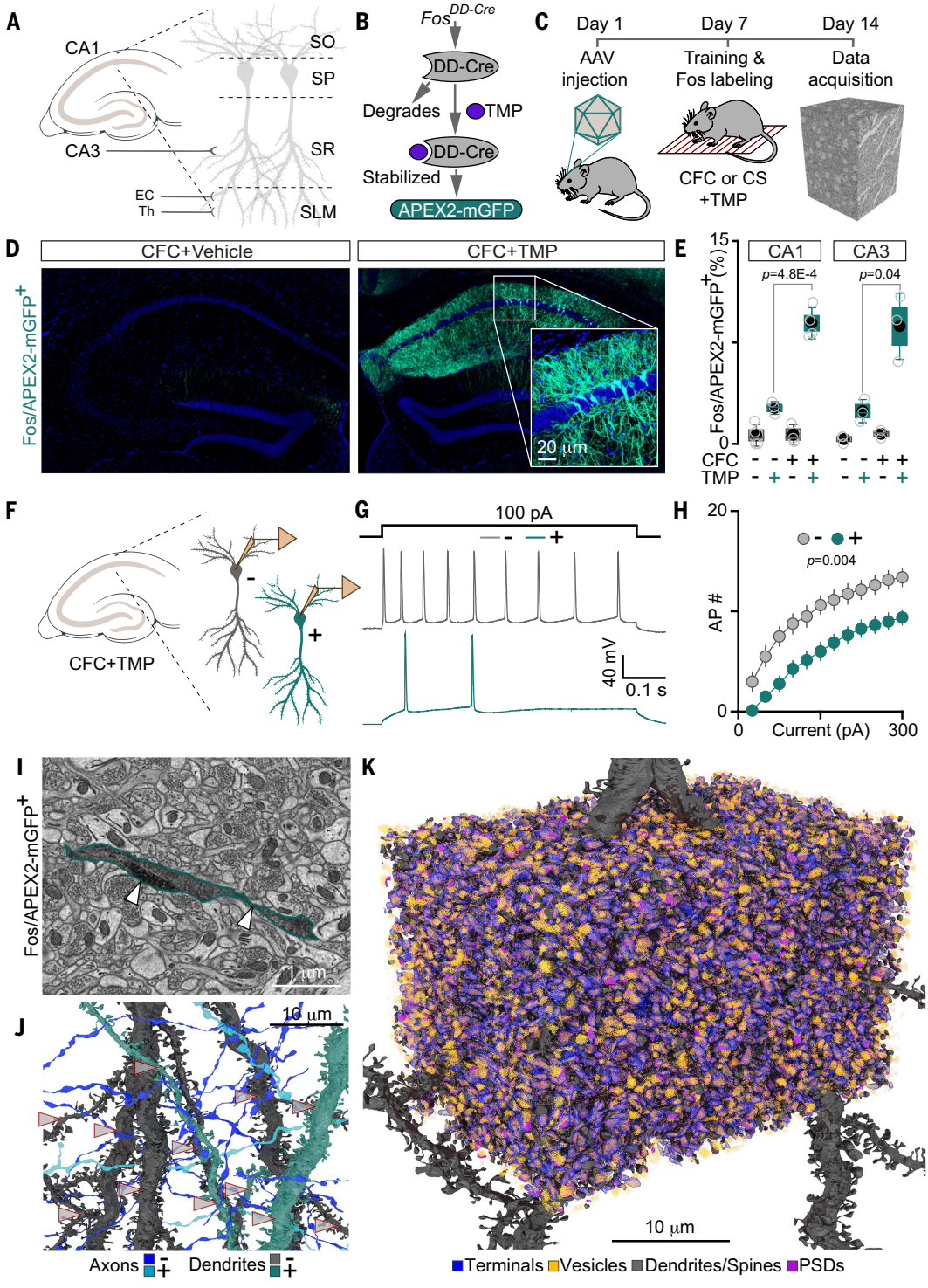

Fig. 1. Workflow for identifying the ultrastructural hallmarks of memory engrams. (**A**) Excitatory pathways in the CA1. SO, stratum oriens; SP, pyramidal cell layer; SR, stratum radiatum; SLM, stratum lacunosum moleculare; EC, entorhinal cortex; Th, thalamus. (**B**) Irreversible labeling of transiently activated neurons with APEX2-mGFP. (**C**) Overview of the experimental design. (**D**) Confocal images of APEX2-mGFP fluorescence in the hippocampi of fear-conditioned $Fos^{DD\text{-}Cre}$ mice. TMP (50 μg/g intraperitoneally) or a vehicle solution was administered 30 min after training. (**E**) Quantifications of reporter-positive (+) cells in areas CA1 and CA3. No CFC + vehicle, n = 4 mice; no CFC + TMP, n = 3; CFC + vehicle, n = 3; CFC+ TMP, n = 4. In this and similar panels, graphs display individual data points (open circles), mean values (filled circles), SEs (boxes), SDs (vertical whiskers), and medians (horizontal lines). P values were calculated using t tests. (**F** to **H**) Electrical properties of (−) and (+) CA1 PNs assessed 7 days after CFC. (F) Schematic of whole-cell recordings. (G) Representative traces of evoked action potentials (APs). (H) Number of APs (mean ± SEM), plotted relative to stimulus intensity. n = 3 mice/8 neurons per group. P value was determined by t test. (**I**) Example of APEX2 tracing in a 2D-EM micrograph (axonal fiber marked by arrows). (**J**) 3D views of (−) and (+) SchC axons and dendrites (arrows) in the CA1sr of fear-conditioned mice. Only a few unlabeled projections are shown. (**K**) Saturated reconstruction of excitatory synapses in ~1/9 of the typical 3D stack used for analysis. (See also Movie 1, figs. S1 to S7, and data S1.)

persist beyond the early phases of memory encoding but precede systems consolidation, when new memories are believed to gradually integrate into the neocortex, rendering the hippocampus no longer necessary for their recall (*10*, *40*). AAVDJ-DIO:APEX2-mGFP was injected into the CA3 and CA1 to label coactivated PNs in both areas. We focused exclusively on excitatory circuits, omitting occasionally labeled GABAergic interneurons. The rationale for this strategy is elaborated below and in the accompanying supplementary materials.

We optimized the protocol for reliable induction of APEX2-mGFP with a single dose of TMP. The drug was administered through peripheral intraperitoneal injection 30 min after training to allow for DD-Cre transcription and translation. Imaging of green fluorescent protein (GFP) fluorescence in hippocampal sections confirmed that the method worked as designed. APEX2-mGFP expression was TMP dependent and up-regulated by CFC. In fear-conditioned mice, the number of APEX2-mGFP–positive neurons in the pyramidal cell layers of CA1 and CA3 increased ~3.6-fold compared with control TMP-treated mice, rising from ~2.5% to ~9% of the total populations (Fig. 1,

D and E). Side-by-side whole-cell current-clamp recordings from labeled (+) and neighboring unlabeled (−) CA1 PNs in acute brain slices showed that (+) PNs had higher thresholds for action potential firing, indicating lower intrinsic excitability (Fig. 1, F to H). This shift was not an artifact of viral transduction itself, because no apparent differences in electrical properties between (+) and (−) PNs were detected when APEX2-mGFP was randomly expressed from the same AAV under the control of constitutive *Camk2*^{Cre} (fig. S3, A to C). However, PNs with a remote history of activity elicited by CFC did not exhibit widespread alterations in excitatory synaptic strength, as evidenced by voltage-clamp recordings assessing the probability of synchronous transmitter release from glutamatergic terminals and the amplitudes of evoked postsynaptic currents mediated by the AMPA and NMDA receptors (fig. S3, D to H).

Reconstruction of excitatory circuits in the CA3-CA1 pathway

We sampled ~110,000 μm^3 SBEM stacks from the CA1sr of *Fos*$^{DD-Cre}$ mice, in which APEX2-mGFP was induced with TMP after exposure to the same novel environment with or without foot shocks to distinguish the impacts of negative valence stimuli that prompt associative learning (CFC) from neutral conditioned stimuli (CS) alone. To ensure that fear-conditioned animals had a retrievable memory at the time of tissue collection, freezing behavior was assessed in separate cohorts from both groups upon their return to the original context (fig. S4). Because prior studies have shown that ensembles marked by *Fos* after memory acquisition and recall are largely segregated across the brain (*8*, *12*), we did not use the retrieval protocol for reconstructions. This approach avoided the challenge of interpreting datasets in which the pools of initially activated PNs included an unknown number of cells that may or may not have been reactivated. The 3D-EM stacks were aligned from raster images with 4-nm pixels, 2-μs dwell time, and 60-nm Z steps (Fig. 1I and fig. S5). Each stack contained ~200,000 synapses.

To expedite image processing, we built a pipeline for segmenting subcellular structures that integrated software packages commonly used in connectomics (*20*, *41*, *42*) with an enhanced version of CDeep3M, the convolutional neural network developed in our laboratories (*43*, *44*). This AI-based platform was tailored for retraining on manually segmented ground truth labels to generate predictions of plasma membranes, axonal and dendritic shafts, nerve terminals, dendritic spines, postsynaptic densities (PSDs), and intracellular organelles. The accuracy of these predictions was verified by benchmarking against manual reconstructions from our own and previously published datasets (*27*) (Movie 1; Fig. 1, J and K; and figs. S6 and S7). Excitatory circuits were reconstructed using the following criteria: (i) Each synapse was assigned a unique ID with Euclidean coordinates; (ii) datasets were categorized by histories of activity on pre- and/or postsynaptic sides, as revealed by peroxidase staining of SchC axons and CA1 PN dendrites (Movie 2 and Fig. 1, I and J); (iii) morphological features of (−) and (+) PNs were compared within specimens and in different mice; (iv) because the (+) PNs were vastly outnumbered by (−) PNs (Fig. 1E), we made a random selection of corresponding internal controls for quantifications to prevent heteroscedasticity; and (v) when choosing statistical methods, we took into account that distributions of most structural brain parameters have asymmetrical lognormal shapes (*45*, *46*).

PNs allocated to an engram do not exhibit stable rearrangements of individual synaptic sites or show a preference for wiring with each other

To begin elucidating the principles of connectivity among PNs resembling initial engrams in the CA3-CA1 pathway, we examined reconstructions of the CA1sr from mice subjected to

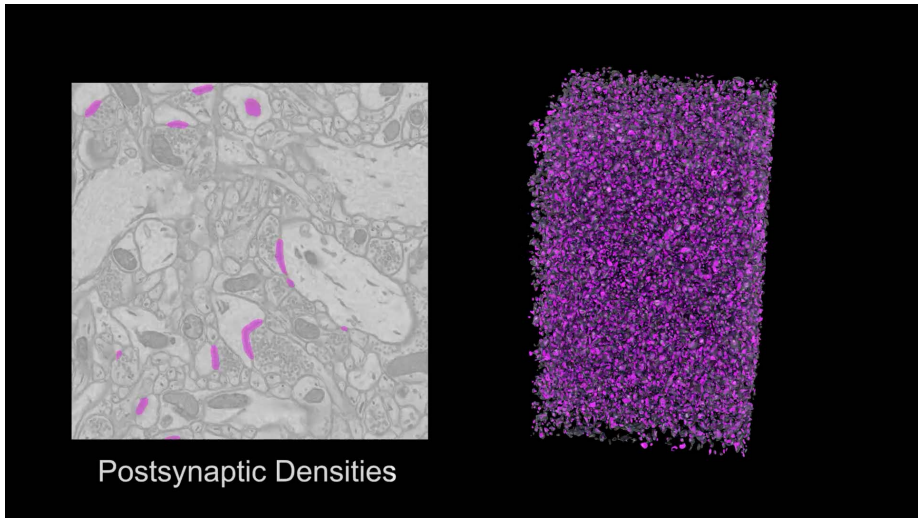

Movie 1. Automatic machine learning–based segmentation of subcellular structures. Left, the animation scrolls through the original 3D-EM image stack acquired from the CA1sr region, displayed at high magnification. The templates for different subcellular structures, used for training convolutional neural networks, are color coded as indicated in the captions. Right, saturated reconstructions of the structures from the left panel, representing ~1/9 of the typical ~110,000 μm^3 sample. Semantic segmentation of synapses and intracellular organelles was performed using CDeep3M in combination with PyIMOD. PyTorch Connectomics was used for instance segmentation of projections.

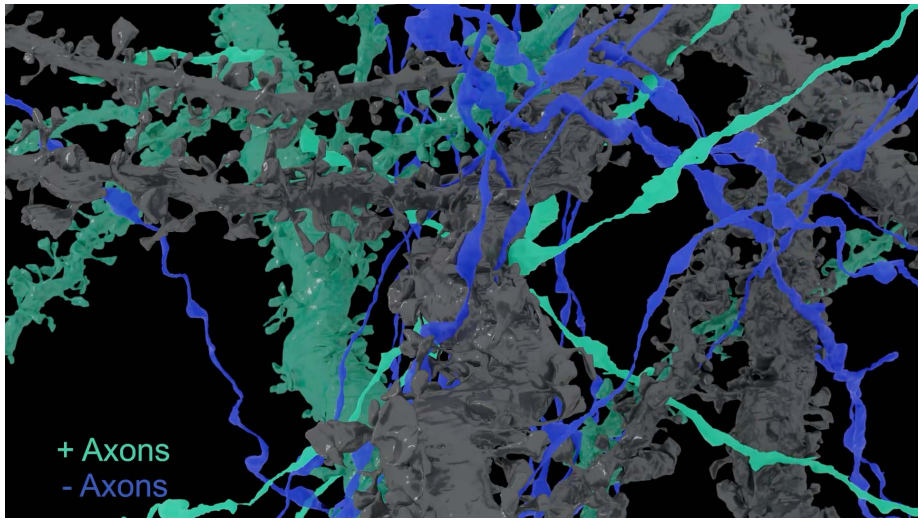

Movie 2. Examples of reconstructed axons and dendrites. Zoomed-in 3D views of dendritic branches of CA1 PNs and incoming SchC axonal fibers in the CA1sr. Fos/APEX2-mGFP-positive (+) processes of PNs activated during associative learning, as well as processes from (−) PNs, are pseudocolored as indicated in the captions and Fig. 1J. Only a few (−) processes are displayed for clarity.

CFC (Fig. 2A). First, we focused on the dendrites of CA1 PNs and mapped their spines, the postsynaptic compartments that cluster receptors and other signaling molecules near sites of transmitter release from opposing axonal terminals (Movie 3, Fig. 2B, and fig. S8). Sensory experience promotes the growth of new spines in many cortical and hippocampal neuron subtypes, but the long-term consequences of this growth on wiring of the adult brain are uncertain, because de novo spinogenesis appears to be counterbalanced by spine elimination (*3*, *47*–*49*). Our analysis showed that the spatial distributions and total spine counts on the dendritic arbors of (–) and (+) CA1 PNs were nearly indistinguishable (Fig. 2C). We then mapped the presynaptic terminals along SchC axonal fibers coming from the CA3 (Movie 4; Fig. 2D; and fig. S9, A and B). Given that the distances between neighboring terminals are more than 10 times greater than those between spines, we measured their lengths with an algorithm that accounts for variability in axonal curvature. Again, the distributions and total terminal counts on (–) and (+) axons were nearly identical (Fig. 2E). To determine whether task-specific coactivation of CA3 and CA1 PNs could be attributed to their preference for wiring with each other, we simultaneously traced the reporter in SchC fibers and their postsynaptic partners within local receptive fields (Movie 4, Fig. 2F, and fig. S9C). The majority (~85%) of terminals formed by (+) fibers contacted the spines of (–) dendrites, and the overall connectivity of (–) and (+) axons was similar (Fig. 2G). Additionally, (–) and (+) axons had comparable branching and innervated the full spectrum of morphologically diverse spines, albeit the fractions of thin (T)- and mushroom

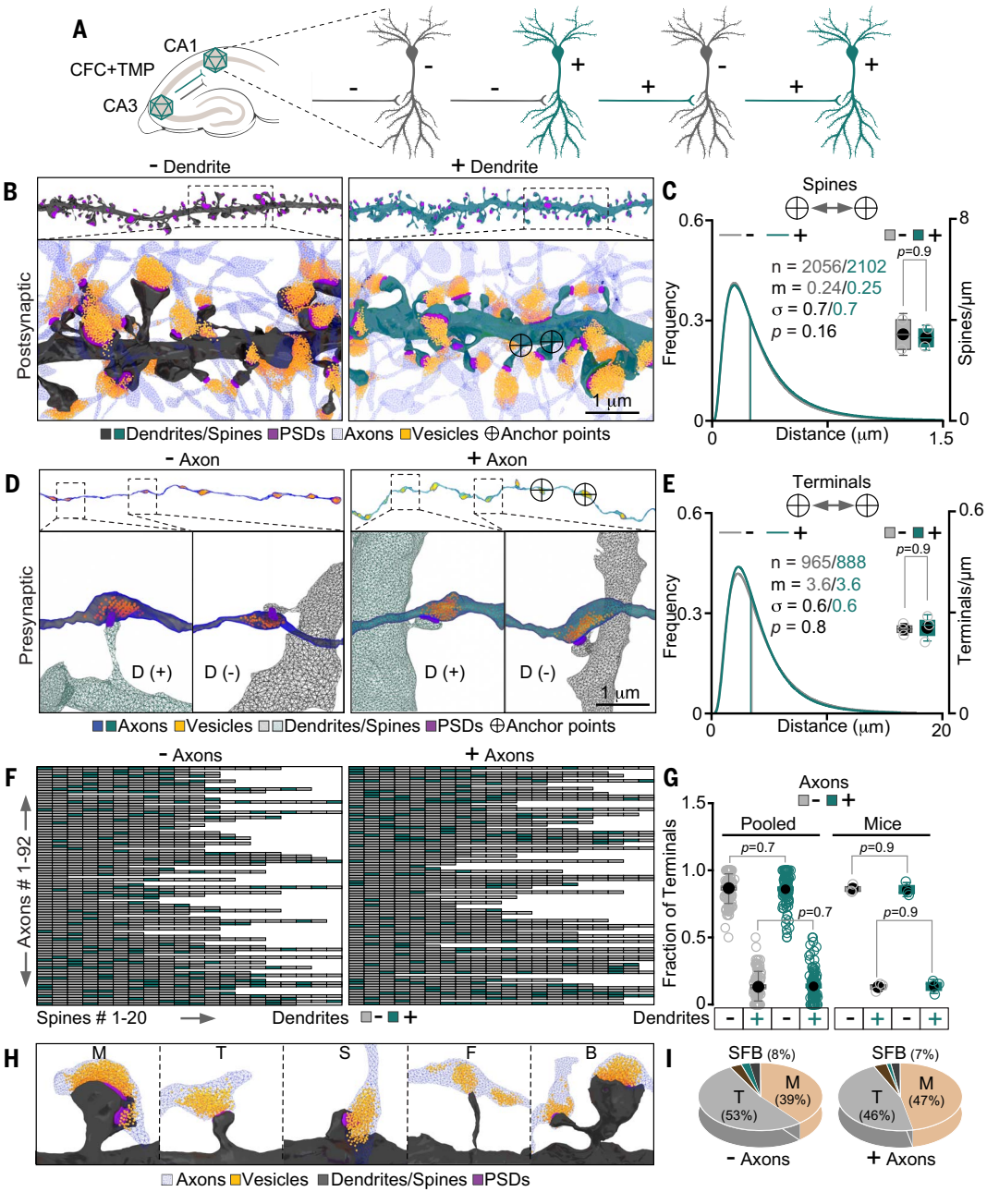

Fig. 2. Synaptic networks of PNs in the CA3-CA1 pathway. (**A**) Schematic of experience-dependent labeling and potential connectivity between (–) and (+) PNs in the CA1sr of fear-conditioned mice. (**B**) 3D views of dendritic branches of CA1 PNs. Enlarged images display local connectomes. Anchor points exemplify the Euclidian coordinates of spines. (**C**) Distributions of distances between spines (lognormal curves with fitting parameters; in this and similar panels, sample sizes (n), medians (m), SDs of logarithmic values (σ), and *P* values are indicated) and the total spine counts per dendrite length, assessed across different mice (box with data overlap plot on the right). (**D**) 3D views of SchC axons of (–) and (+) CA3 PNs. Magnified images display pre- and postsynaptic structures. D, dendrites. (**E**) Distributions of distances between terminals along individual axons and total terminal counts per fiber length. (**F**) Heatmaps representing the wiring of (–) and (+) axons with (–) and (+) dendrites. The color-coded boxes in vertical columns denote single spines. (**G**) Fractions of terminals formed on dendrites of (–) and (+) CA1 PNs. (**H**) Examples of synapses with morphologically distinct spines. M, mushroom; T, thin; S, stubby; F, filopodia; B, bifurcated. (**I**) Fractions of M-, T-, S-, F-, and B-type spines innervated by (–) and (+) axons. All quantifications are from three separate mice. *P* values were calculated using Mann-Whitney tests for distribution fits and *t* tests with Welch correction for box plots. (See also Movies 2 to 4, figs. S8 and S9, and data S2.)

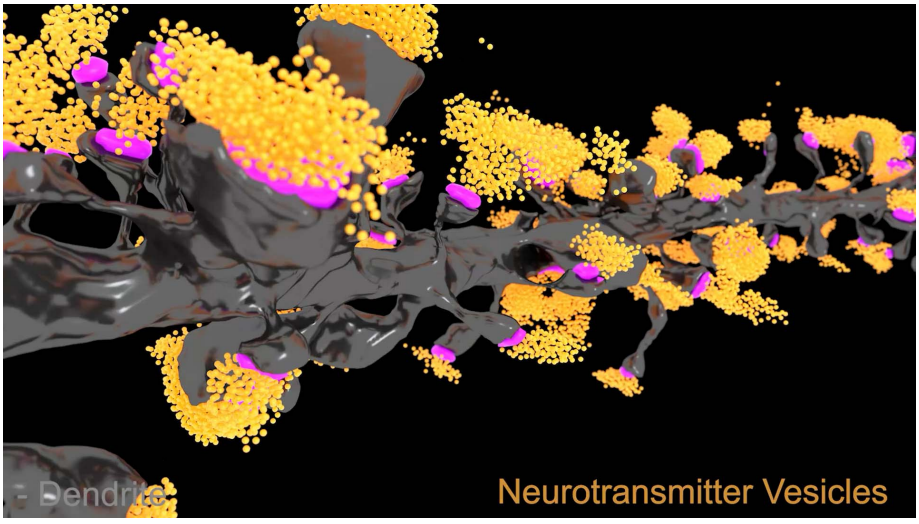

Movie 3. Local synaptic networks in the CA1sr. Zoomed-in 3D views of microconnectomes of (+) CA1 PNs representing initial engrams and randomly selected neighboring (−) PNs are shown side by side. The animation displays dendritic branches with spines, PSDs, and opposing axonal terminals containing neurotransmitter vesicles. Structures are color coded as indicated in the captions and Fig. 2B.

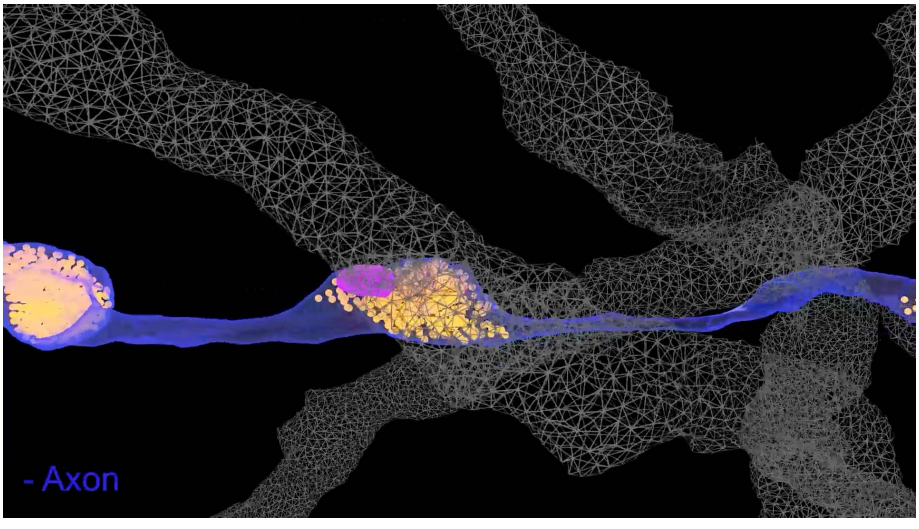

Movie 4. Axonal wiring in the CA1sr. Zoomed-in 3D views of individual (+) axonal fibers of CA3 PNs representing initial engrams and randomly selected neighboring (−) fibers are shown side by side. The animation displays axons crossing receptive fields and innervating different dendritic branches of CA1 PNs. Structures are color coded as indicated in the captions and Fig. 2D. Note that (+) PNs coactivated during associative learning do not show a preference for wiring with each other.

(M)-type spines were slightly uneven (Fig. 2, H and I, and fig. S9, D and E).

Initial engram ensembles expand their connectomes through MSBs

Although the bulk of en passant synapses of long-range glutamatergic axons have one-to-one spine-to-terminal ratios, some terminals connect to multiple spines, usually residing on different dendritic arbors (*50*–*52*). Because of their potential to synchronize outputs to several downstream targets, these atypical multisynaptic boutons (MSBs) are believed to enhance network excitation coherence and coordinate the induction of Hebbian plasticity for sensory processing and learning (*52*–*57*). However, the precise functional roles of MSBs, the mechanisms underlying their morphogenesis, and their contribution to the assembly of cellular substrates of memory traces are unclear. Because PNs with a remote history of activity correlating with learning showed no changes in the number or arrangement of isolated terminals and spines (Fig. 2, C and E), we predicted that engram formation might involve a shift in the balance between conventional single-synaptic boutons (SSBs) and MSBs. To test this, we identified MSBs in pre-annotated connectomes and studied their origins, morphologies, and synaptic target selectivity (Movie 5 and Fig. 3A).

MSBs were present on both the (−) and (+) SchC axons of fear-conditioned mice, but their counts were ~1.6-fold higher on (+) axons. Consequently, (+) axons exhibited a proportional loss of SSBs, and their total spine-to-terminal ratios were increased by ~19% (Fig. 3, B and C, and fig. S10, A and B). Moreover, (+) MSBs were coupled with ~50% larger fractions of all innervated spines than their (−) counterparts because of differences in both MSB abundance and their complexity (Fig. 3, D and E). Approximately 26% of (+) MSBs contacted more than two spines, representing an ~2.4-fold increase from the 11% in (−) controls. The maximum number of spines per MSB also rose from four to six (Fig. 3F). These effects expanded the local connectomes of (+) axons, as demonstrated by quantifications of separate dendritic branches receiving inputs from each terminal, fractions of compound synapses formed by SchC fibers onto neighboring spines on the same dendrite, and the number of different dendrites with spines that were contacted by each MSB (Fig. 3, G to I). None of these changes occurred in mice exposed to a neutral CS, indicating that axonal networks in the CA1sr are reorganized through MSBs in a stimulus-specific manner (Fig. 3, B to I). Thus, the restructuring of excitatory circuits observed after CFC is likely a signature of associative learning rather than the outcome of generic excitation of PNs or the *Fos*-driven expression of APEX2-mGFP per se. Nonetheless, the MSB target selection was not biased toward coactivated CA1 PNs. Consistent with our initial assessment of wiring diagrams (Fig. 2, F and G), ~85% inputs from MSBs of (+) axons of fear-conditioned mice were provided to (−) dendrites (Fig. 3, J to K, and fig. S10, C and D). Although the numbers of (−) and (+) MSBs on (+) dendrites were marginally mismatched (fig. S10E), this mismatch simply reflected the unequal MSB availability.

Memory encoding correlates with input-specific up-scaling of glutamatergic synapses

Considering that physical connectivity alone does not definitively predict population coding in a network, we next investigated the impact of negative valence and neutral stimuli on the structure of glutamatergic synapses (Movie 6). To establish the relationship between PN activation and the properties of their individual connections, we extrapolated synaptic weights by fitting the lognormal distributions of spine head and nerve terminal volumes. These parameters are generally indicative of functional strength; for instance, spines enlarge during long-term potentiation and shrink during long-term depression (*47*, *58*). In agreement

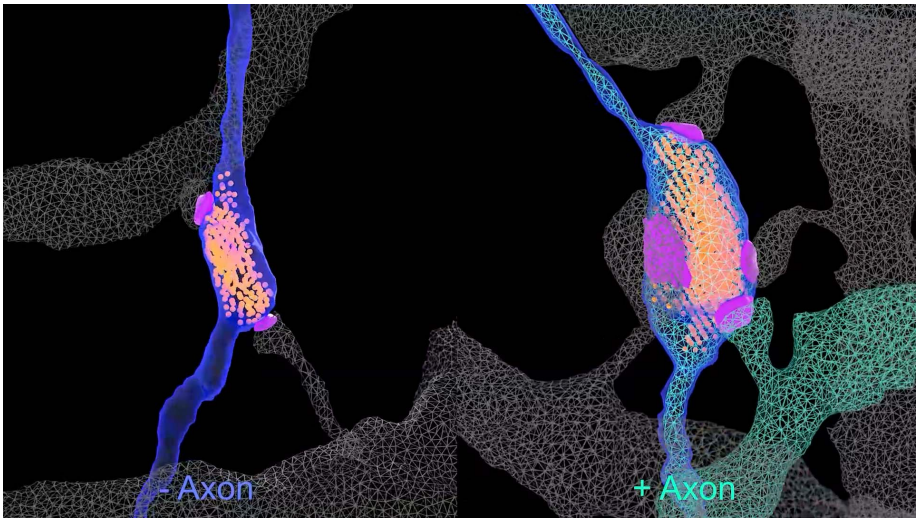

Movie 5. Examples of individual MSBs. Side-by-side 3D views of MSBs formed by (+) axons of CA3 PNs representing initial engrams and randomly selected neighboring (−) axons. The animation highlights terminals filled with neurotransmitter vesicles as well as target dendrites with innervated spines and PSDs. Structures are color coded as indicated in the captions and Fig. 3A. Note that (+) MSBs are associated with a greater number of spines.

with electrophysiological recordings of AMPA currents (fig. S3), (−) and (+) CA1 PNs of fear-conditioned mice had no detectable differences in spine head volumes, as assessed across dendritic branches of parent neurons irrespective of axonal labeling. However, of the two dispersed spine populations categorized solely by the activity history of contacting axons, the spines innervated by (+) SchC fibers were enlarged (fig. S11, A to C). The axonal terminals of (+) CA3 PNs activated by CFC were also markedly bigger (fig. S11, D and E). The volumes of post- and presynaptic compartments were unaltered in (+) PNs of mice subjected to CS (fig. S11, F to I).

To explore the implications of this learning-related upscaling within the framework of the Hebbian rule, we extrapolated the weights of synapses categorized into four groups based on experience-dependent labeling on both sides. The size distribution profiles of (−/+) spines, representing postsynaptic induction only, were comparable to those of (−/−) controls. By contrast, the distributions for (+/−) and (+/+) populations were right-shifted, with an ~1.3-fold increase in median sizes in each pool (Fig. 4A). A similar relationship was observed in axonal terminals, with only a slight difference in median values between the (+/−) and (+/+) groups, corresponding to a ~1.8- and ~1.9-fold increase, respectively (Fig. 4B). Additional analysis revealed that input-specific augmentation of pre- and postsynaptic weights occurred regardless of bouton type (Fig. 4, C to F and fig. S11, J to Q). However, the enlargement of previously activated synapses was accompanied by nonuniform changes in structural variability. The head volumes of spines innervated by (+) SSBs and MSBs of fear-conditioned mice were less variable, as indicated by the SDs of logarithmic values (σ) (Fig. 4, A, C, and E, and fig. S11, C, J, and K). Conversely, the volume variability of (+) terminals was greater, but this effect was confined to MSBs (compare σ values and medians in Fig. 4, B, D, and F, and fig. S11, E, L, and M).

To elucidate these discrepancies, we examined the relationships between terminal sizes and the sizes of spines, PSDs, and axon-spine interfaces (ASIs) in single synapses. The volumes of SSBs formed by (−) axons strongly correlated with those of their contacted spines, PSDs, and ASIs (Spearman rs = 0.64 to 0.66), whereas the pairwise correlations of these parameters in (−) MSBs were only moderate (rs = 0.44 to 0.46). These differences were even more pronounced in synapses of previously activated CA3 PNs, with rs = 0.45 to 0.48 for (+) SSBs compared with rs = 0.12 to 0.21 for (+) MSBs. In both cases, the correlations weakened due to asymmetrically enlarged terminals (Fig. 5, A to C, and fig. S12). The structural proportionalities of (+) MSBs were independent of the coactivation status of CA1 PNs, further indicating that the distribution of synaptic weights in an engram is governed by mechanisms that appear non-Hebbian at the cellular level (compare Fig. 5, D to F, with Fig. 5, A to C). The lower σ values of enlarged spines innervated by all terminals of (+) axons likely reflect the matching of postsynaptic weights for optimal population coding. Conversely, the loss of proportionality of (+) MSB with isolated spines could be attributed to higher complexity of target interactions. Indeed, the sizes of presynaptic boutons and the number of neurotransmitter vesicles in each bouton strongly correlated with the number of innervated spines (Pearson r = 0.84 to 1.0), suggesting that MSBs expand to maintain efficient neurotransmission with an increasing number of postsynaptic partners (Fig. 5, G and H).

Synapses activated during associative learning have modified mitochondria and SER

To gain additional insights into the structural determinants of glutamatergic synapses of PNs recruited for memory storage, we focused on the membrane organelles essential for energy metabolism, protein synthesis, and intracellular calcium signaling: mitochondria and the smooth endoplasmic reticulum (SER) (Movie 7; Fig. 6, A and B; and fig. S13, A to C). In addition to supplying ATP for SNARE-mediated vesicle recycling, small mitochondria anchored at presynaptic boutons modulate neurotransmitter release kinetics by buffering free calcium (*59*–*61*). By contrast, the typically elongated mitochondria found in dendritic shafts rarely extend into spines (*20*). Postsynaptic calcium homeostasis and local translation in spines are thought to be regulated by a specialized part of the SER network known as the spine apparatus (SA) (*62*, *63*). Many excitatory synapses lack mitochondria and SA (*44*, *64*), but the reasons for this heterogeneity are poorly understood. Previous EM studies suggested that the subcellular localization of these organelles may be influenced by sensory stimuli; however, this hypothesis is based on indirect observations from electrically stimulated brain slices and mice with widespread loss of glutamate secretion throughout development (*44*, *64*). Our reconstructions revealed that the percentages of terminals containing mitochondria ranged between ~27% and ~56% in the CA1sr of mice subjected to CFC or CS. These organelles were more likely to be anchored in MSBs than in SSBs (fig. S13, D to F). Because efficient calcium buffering is necessary for synchronizing vesicular release, and this process depends on both the anchoring of mitochondria in axons and their size (*65*, *66*), we investigated whether these organelles undergo compensatory swelling in the enlarged terminals of PNs activated by CFC. Such a mechanism could be particularly important for MSBs, in which vesicles from a shared pool undergo exocytosis at multiple sites. Supporting this prediction, the median mitochondrial volumes were increased by ~1.3-fold in terminals of (+) SchC axons (Fig. 6C). The presynaptic mitochondrion size was proportional to both terminal size (Spearman rs = 0.45 to 0.52) and the number of contacted spines (Pearson r = 0.85) (Fig. 6, D and E). On the contrary, spines innervated by (+) axons exhibited a notable, CFC-specific loss of SA (Fig. 6F). This loss occurred regardless of bouton type or the activity history of parent CA1 PNs,

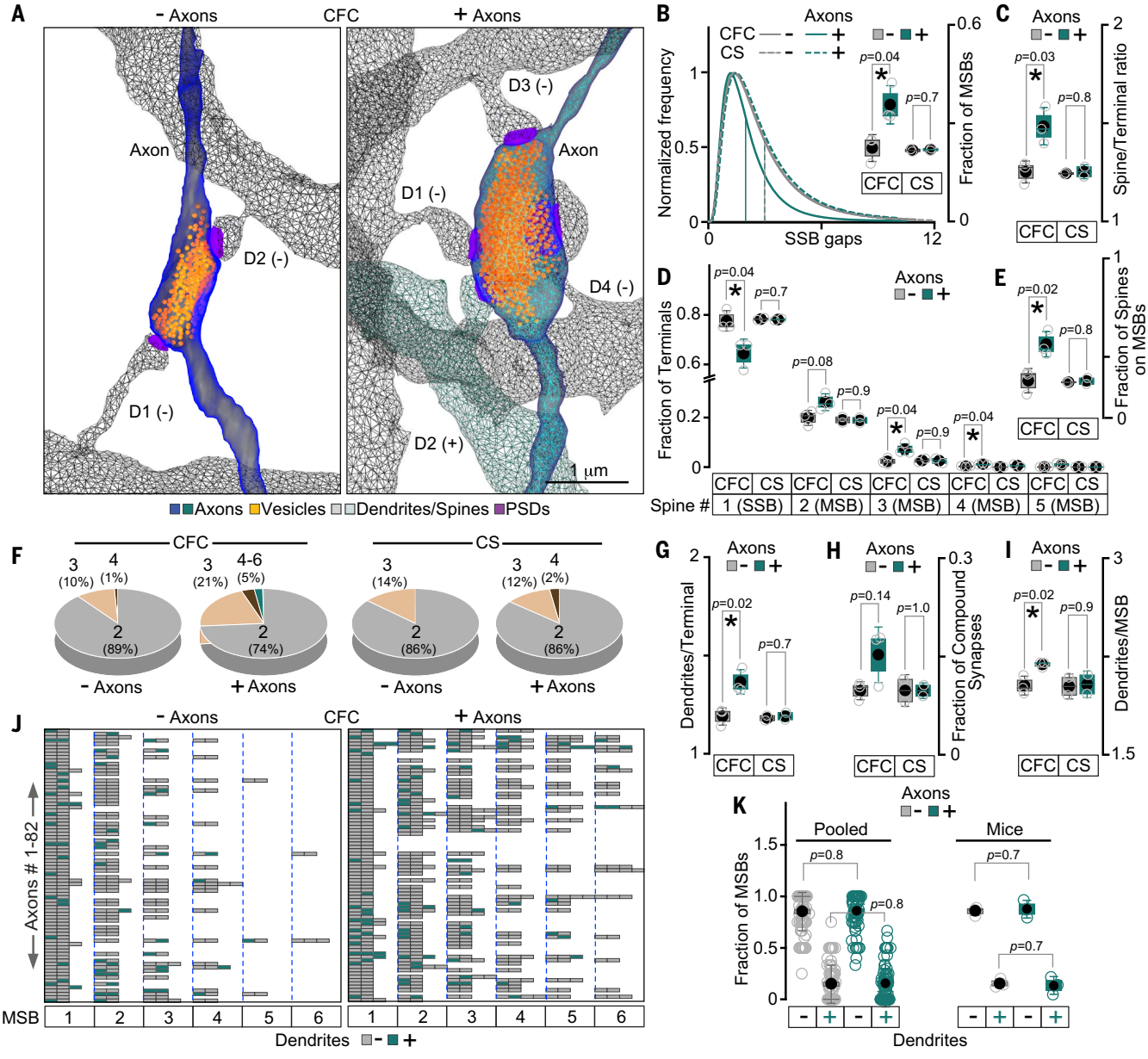

Fig. 3. Expansion of PN connectomes through MSBs. (**A**) 3D views of MSBs of (−) and (+) SchC axons connecting to distinct dendrites (D1 to D4) of CA1 PNs in fear-conditioned mice. (**B** to **I**) Long-term effects of presynaptic activity associated with CFC (n = 3 mice) or CS (n = 2). Datasets were categorized based on axonal labeling. (B) Count distributions of SSBs between MSBs (SSB gaps) and averaged fractions of MSBs relative to SSBs on each axon, as determined in individual mice. (C) Overall spine-to-terminal ratios for (−) and (+) axons. (D) Fractions of terminals contacting the indicated numbers of spines. (E) Fractions of spines contacted by MSBs. (F) Percentages of MSBs innervating different numbers of spines, ranging from two to six. (G) Number of dendrites innervated by individual terminals. (H) Fractions of compound synapses. (I) Number of different dendrites innervated by MSBs (excluding compound synapses). (**J** and **K**) Analysis of MSB networks in fear-conditioned mice (n = 3). (J) Heatmaps representing axonal wiring through MSBs. Each box in the vertical columns shows the number of color-coded postsynaptic counterparts of each MSB formed by individual axons (SSBs are omitted). (K) Fractions of MSBs of (−) and (+) axons connecting to (−) and (+) dendrites. P values were calculated using t tests with Welch correction. (See also Movie 5, fig. S10, and data S3.)

although P values for comparisons between two pairs of mice did not reach statistical significance (Fig. 6, G to J). Thus, presynaptic activity correlated with learning appears to differentially affect organelles that maintain synaptic homeostasis and define the propensities for short- and long-term plasticity by enhancing the local function of axonal mitochondria while disabling the SA in spines.

Learning-related presynaptic activity promotes the interfacing of nerve terminals with astrocytes

Astrocytes play multifaceted roles in the brain by regulating synapse formation and elimination, clearing neurotransmitters from the extracellular space, maintaining ion homeostasis, supplying glucose, and signaling to neurons through secreted factors (*67*, *68*). Furthermore, functional cross-talk between neurons and astrocytes has been shown to influence synaptic plasticity and memory (*69*, *70*). To investigate the relevance of physical interactions between synapses and astrocytes in associative learning, we automatically segmented astrocytes in the CA1sr of mice exposed to CFC or CS. The prediction maps were verified by the presence of glycogen deposits and used to

quantify the number of terminals contacting astrocytic processes, as well as the volumes of astrocyte-terminal interfaces (ATIs) (Movie 8; Fig. 7, A and B; and fig. S14, A and B). The datasets were categorized by axonal labeling as the frame of reference. The mesh of astrocytic processes surrounding projections and synapses was highly complex (Movie 8 and Fig. 7, A and B). The proportion of SSBs and MSBs interfacing with these processes ranged from ~50% to ~85% (Fig. 7, C and D, and fig. S14C). The distributions of ATI volumes were exponential rather than log-normal, possibly due to the more stochastic nature of contacts, as opposed to neuronal synapses. Median ATI volumes were larger in MSBs than in SSBs, with a pronounced increase in both types of terminals of CA3 neurons activated by CFC (~1.2-fold for SSBs and ~1.5-fold for MSBs; Fig. 7, E and F, and fig. S14D). ATI sizes were proportional to the sizes of individual terminals, although the correlation coefficients and *z*-scores were generally low (Fig. 7, G and H, and fig. S14E). However, ATI sizes strongly correlated with the number of innervated spines (Fig. 7I), suggesting that astrocytic interactions are up-regulated to accommodate increased presynaptic weights and complexity of postsynaptic targets, much like the swelling of axonal mitochondria.

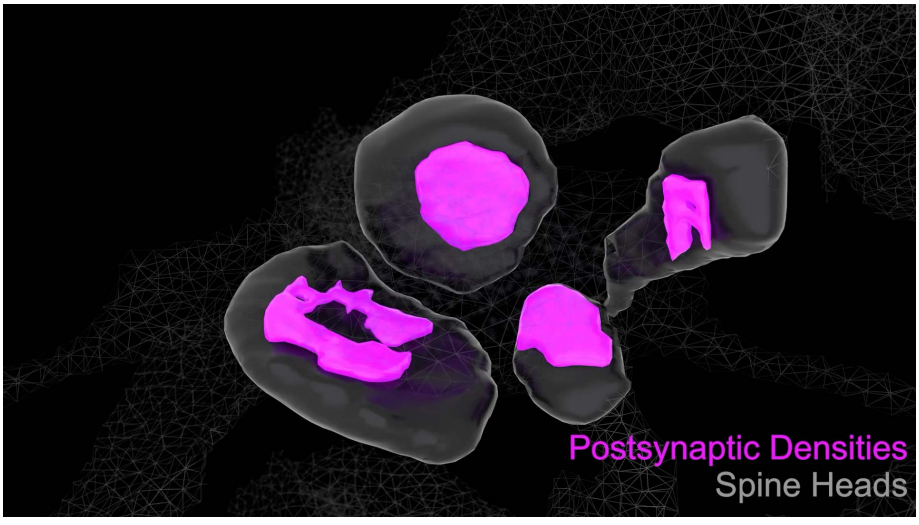

Movie 6. 3D view of core synaptic structures. The animation highlights the boundaries of a MSB filled with vesicles, along with the heads of innervated spines, PSDs, and ASIs used for volumetric measurements, as shown in Figs. 4 to 7 and the accompanying supplementary materials. Structures are color coded as indicated in the captions.

Discussion

In summary, our findings demonstrate that hippocampal PNs recruited during associative learning exhibit increased complexity of connectivity, augmented synaptic weights,

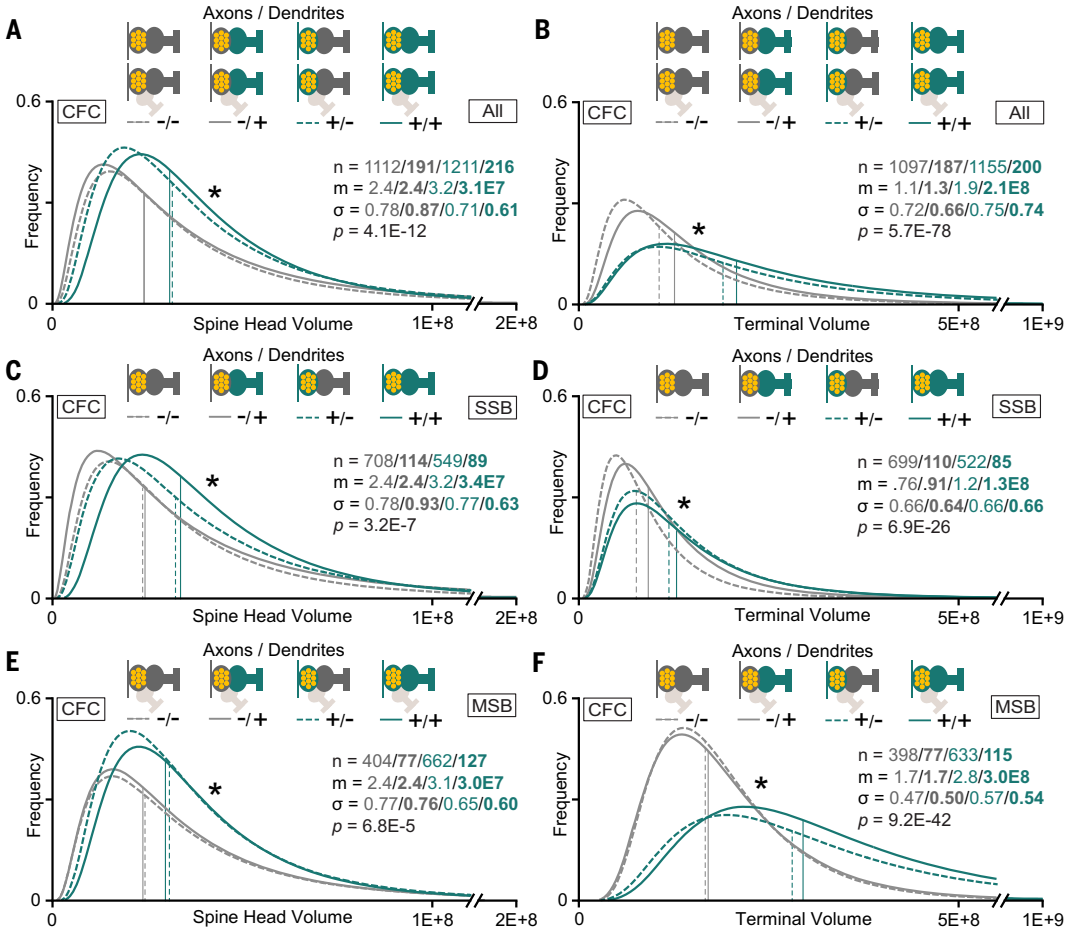

Fig. 4. Relationships between activity patterns and extrapolated synaptic weights. The sizes of individual excitatory synapses were measured in the CA1sr of fear-conditioned mice (n = 3). Panels show lognormal distributions of spine head and terminal volumes with fitting parameters. Each dataset was categorized into four groups, as indicated in the legends. (**A**) Head volumes for all spines on dendrites of (−) and (+) CA1 PNs innervated by (−) and (+) SchC fibers. (**B**) Volumes of all axonal terminals. (**C**) Head volumes of spines contacted by SSBs. (**D**) SSB volumes. (**E**) Head volumes of spines contacted by MSBs. (**F**) MSB volumes. Volumetric measurements are displayed in cubic nanometers. *P* values were calculated using Kruskal-Wallis analysis of variance (ANOVA). Detailed post hoc statistical analyses for individual groups are available in data S4. (See also Movie 6 and fig. S11.)

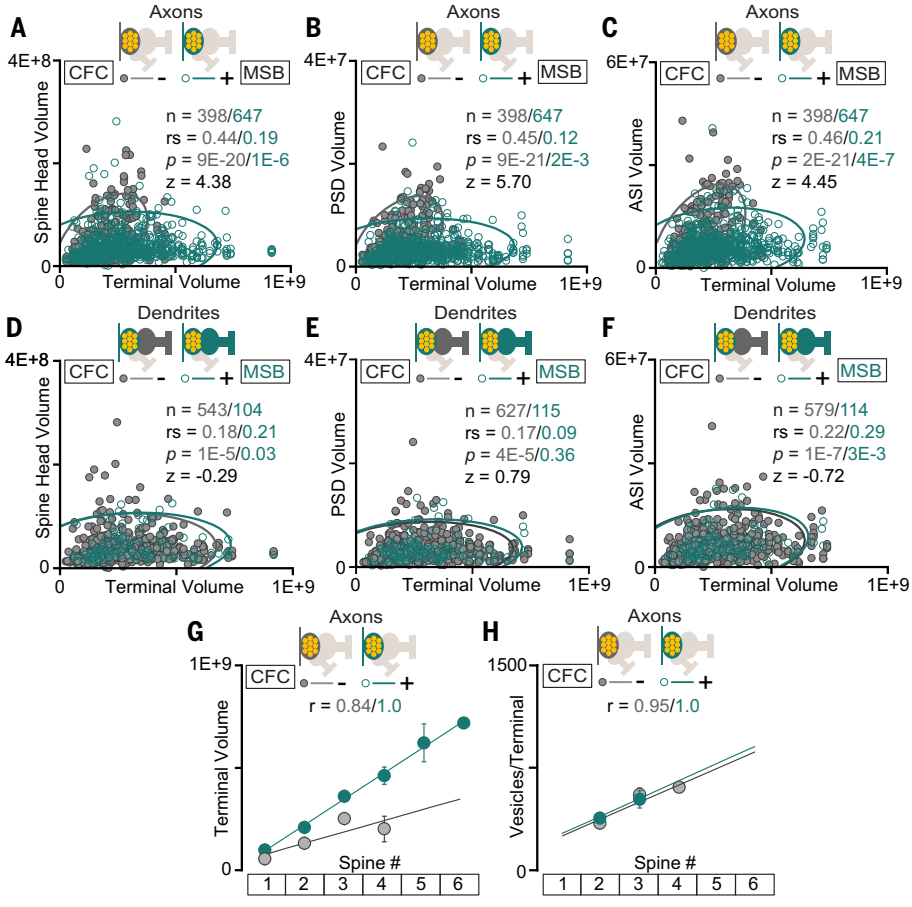

Fig. 5. Structural proportionalities of MSBs. The relationships between the sizes of core structural elements of individual MSB-type synapses were examined in the CA1sr of fear-conditioned mice (n = 3). Datasets were categorized as shown in the legends. (**A** to **C**) Correlations between the indicated parameters in synapses grouped by the activity histories of CA3 neurons. Scatter plots with confidence ellipses, sample sizes (n), Spearman correlation coefficients (rs), Fisher transformation scores (z), and P values are shown. (A) Spine head versus terminal volumes. (B) PSD versus terminal volumes. (C) ASI versus terminal volumes. (**D** to **F**) The same analyses were performed for (+) MSBs innervating (−) and (+) CA1 PNs. (**G** and **H**) Relationships between terminal volumes (G) and vesicle pool sizes (H) and the number of innervated spines (one spine = SSB; two or more spines = MSB). Pearson correlation coefficients (r) are indicated for each comparison. Volumetric measurements are displayed in cubic nanometers. (See also Movie 6, fig. S12, and data S4.)

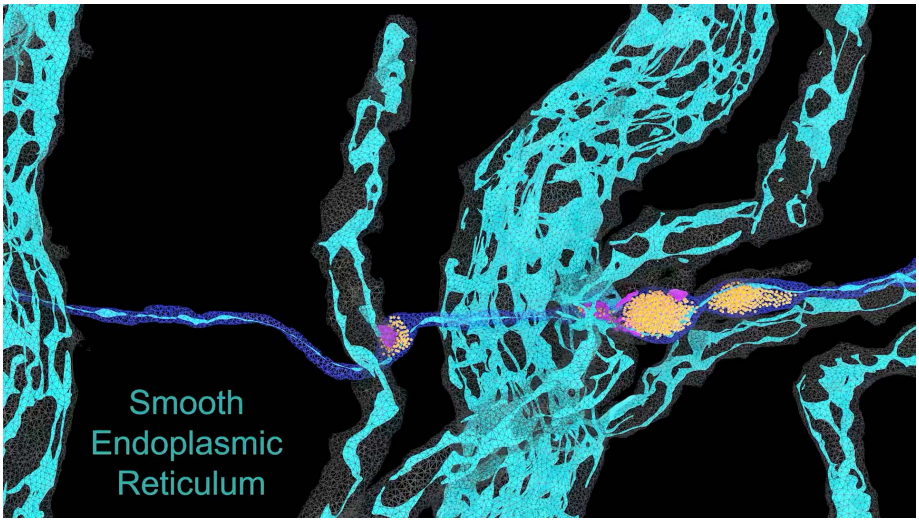

Movie 7. Distributions of neuronal mitochondria and SER. The animation displays mitochondria and SER localized within a single SchC axon and its target dendrites in the CA1sr. A zoomed-in 3D view highlights mitochondria anchored in a presynaptic terminal and SER extending into a spine, forming the SA. Structures are color coded as indicated in the captions and Fig. 6, A and B.

remodeled mitochondria and smooth ER, and enhanced interfacing with astrocytes. Despite their diverse nature, these structural correlates of memory storage share three key features: (i) Their manifestation depends on presynaptic signals associated with negative valence, rather than neutral sensory stimuli; (ii) their expression extends beyond simultaneously activated postsynaptic neurons; and (iii) they involve MSBs.

Previous studies have shown that neuronal populations responding to specific sensory stimuli are not always fixed over time. Evidence for the cellular flexibility of information coding comes from various readouts and model systems, including optical imaging of neural ensembles marked with *Fos*-inducible reporters after Pavlovian conditioning, the same paradigm used in our work (*8*, *12*, *13*). Our observations provide insights into this flexibility. The lack of preferential wiring between PNs activated by CFC and CS suggests that these neurons are part of broader circuits. The learning-related expansion of PN connectomes in the CA1sr is mediated by MSBs, which exhibit greater presynaptic strength compared with conventional boutons. This expansion is accompanied by input-specific enlargement of spines innervated by activated CA3 PNs. Contrary to Hebbian principles, these changes in local wiring diagrams and the weights of individual synapses are not restricted to PNs representing initial engrams. Thus, it is reasonable to predict a low likelihood of reactivating the same ensemble in response to the same cues. Notably, recent brain-wide analyses showed that only 16% of CA1 PNs recruited during fear memory acquisition are reactivated upon recall despite similar ensemble sizes (*12*).

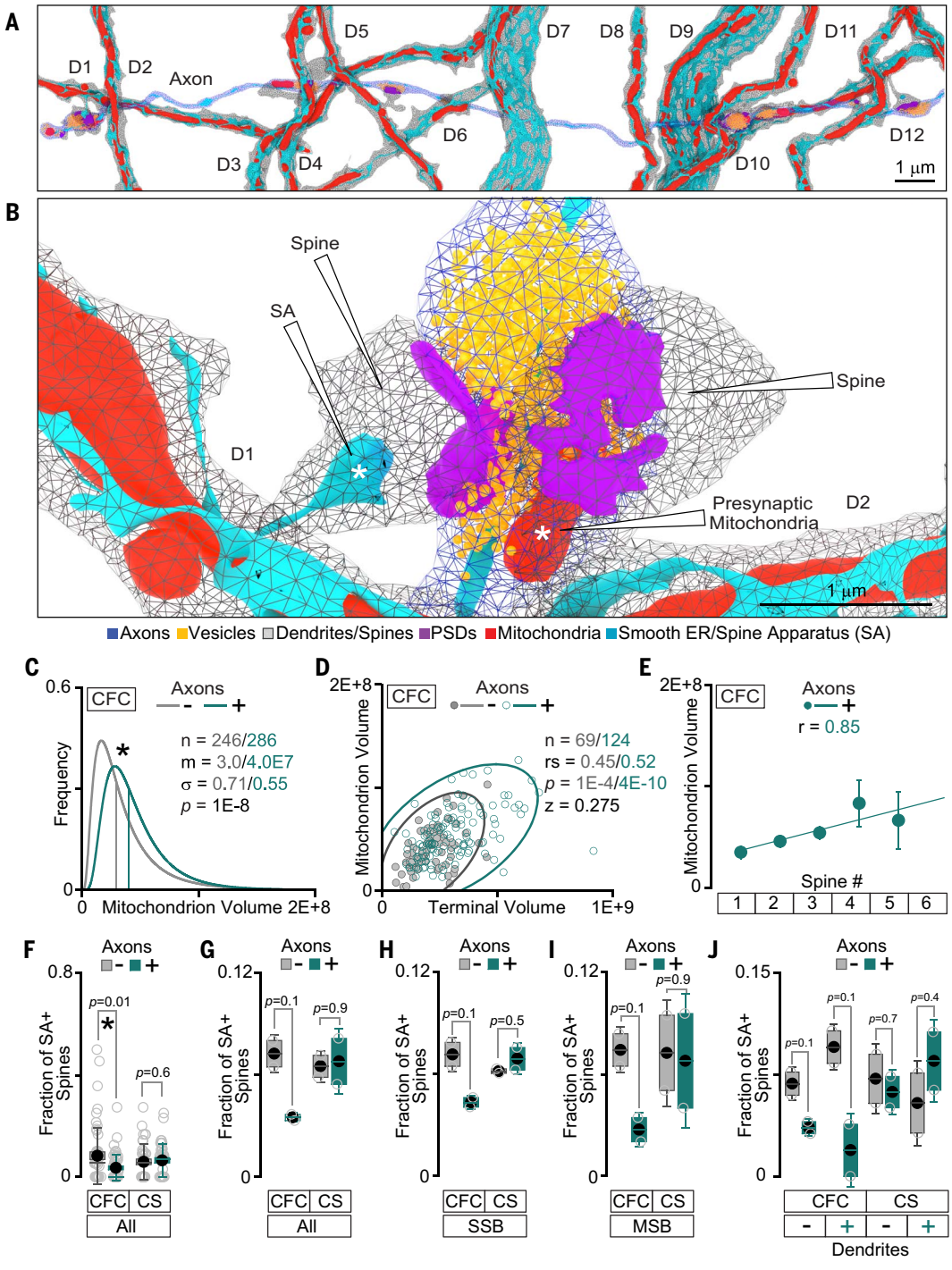

Fig. 6. Reconstructions of mitochondria and SA. (**A**) 3D views of mitochondria and SER in SchC axons and their target dendrites (D1 to D12) in the CA1sr. (**B**) Enlarged image highlighting presynaptic mitochondria and postsynaptic SA. (**C** to **E**) Analysis of mitochondria in terminals formed by (−) and (+) axons of fear-conditioned mice. (C) Distributions of mitochondrial volumes. Graph displays lognormal curves with fitting parameters. (D) Relationships between mitochondrial and terminal volumes. Scatter plots with confidence ellipses, sample sizes (*n*), Spearman correlation coefficients (*rs*), Fisher transformation scores (*z*), and *P* values are shown. (E) Pearson correlation between the volumes of presynaptic mitochondria in (+) axons and the number of innervated spines. (**F** to **I**) Fractions of SA-positive spines innervated by (−) and (+) axons in mice subjected to CFC or CS. Pooled datasets and comparisons between individual animals are shown. (**J**) Fractions of SA-positive spines in synapses subdivided into four groups based on the activity histories of CA3 and CA1 neurons. All quantifications are from two mice per group. Volumetric measurements are displayed in cubic nanometers. *P* values were calculated using Mann-Whitney tests for distribution fits and *t* tests with Welch correction for box plots. (See also Movie 7, fig. S13, and data S5.)

The discovery of experience-dependent synaptogenesis and synapse elimination has popularized the idea that sensory stimuli exert lasting effects on the computational properties of central neurons by altering the number and/or subcellular distribution of synaptic contacts (*1*, *3*, *47*). Our results suggest an alternative mechanism in which neurons engaged in memory encoding diversify their wiring diagrams through MSBs while maintaining the spatial arrangements of isolated pre- and postsynaptic sites. In the CA3-CA1 pathway, this mechanism may enhance the associative capacity to differentiate similar experiences and promote ensemble sharing for memory generalization. Moreover, experience-dependent changes in the balance between MSBs and conventional connections, as well as the architectures of individual MSBs, may serve broader functions: improving the efficiency of temporal coding and increasing network redundancy for reliable information storage and retrieval.

Although we observed a common relationship between PN activity history, organelle content within individual synapses, and their extracellular microenvironment, the physiological consequences of this relationship may differ in nerve terminals and dendritic spines. The restructuring of presynaptic mitochondria and terminal-astrocyte interfaces resembles adaptive changes driven by experience-dependent terminal growth, particularly in MSBs, to maintain presynaptic homeostasis. Our findings

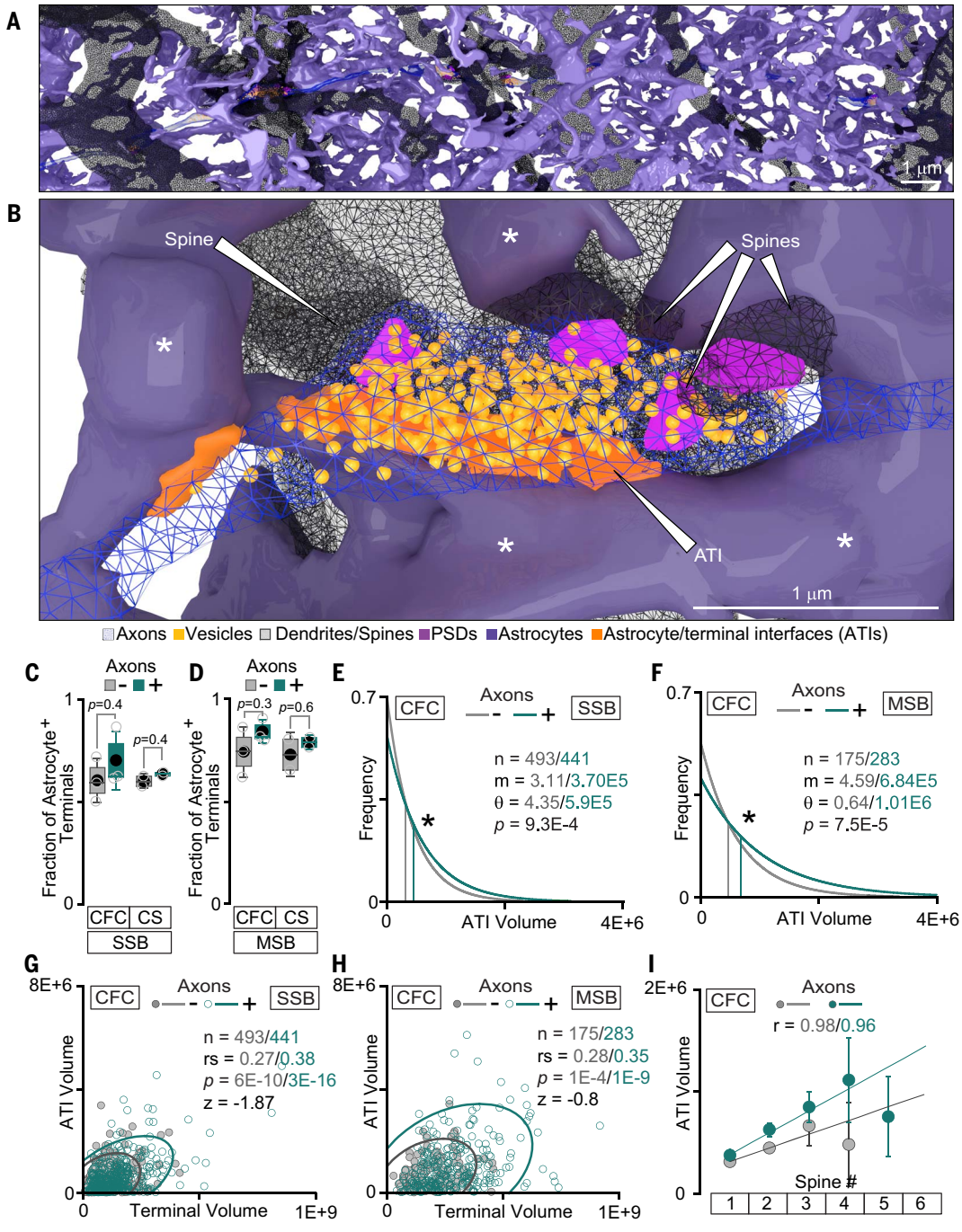

Fig. 7. Interfacing of synapses with astrocytes. (**A**) Saturated reconstruction of astrocytic processes in the CA1sr. (**B**) Enlarged 3D view of astrocytes (denoted by asterisks) contacting an MSB. (**C** and **D**) Fractions of SSB-type (C) and MSB-type (D) synapses with (−) and (+) terminals contacting astrocytes in mice subjected to CFC (n = 3) or CS (n = 2). (**E** to **I**) Quantifications of ATIs in fear-conditioned mice (n = 3). Datasets were categorized by presynaptic label. (E and F) Distributions of ATI volumes for SSBs (E) and MSBs (F) with fitting parameters. (G and H) Spearman correlations between ATI and SSB (G) and MSB (H) terminal volumes. (I) Pearson correlations between ATI volumes and the number of innervated spines. Volumetric measurements are displayed in cubic nanometers. P values were calculated using Mann-Whitney tests for distribution fits and t tests with Welch correction for box plots. (See also Movie 8, fig. S14, and data S5.)

align with deep sequencing studies showing that engram neurons exhibit elevated expression of proteins localized to neurotransmitter vesicles, because the copy numbers of these proteins correlate with terminal and vesicle pool sizes (*71*, *72*). Conversely, the redistribution of the SA is reminiscent of synaptic tagging, a mechanism by which synapses receiving plasticity-inducing stimuli are modified through the local capture of newly synthesized proteins (*63*, *73*–*75*). The loss of SA in enlarged spines innervated by activated CA3 PNs may "lock" these spines in a potentiated state, preventing further modification by subsequent uncorrelated activity.

Limitations of our study, outstanding questions, and future directions

Our work provides a comprehensive nanoscale snapshot of excitatory circuits, but the temporal dynamics of the observed effects remain unresolved. It is unclear whether the synaptic networks of PNs allocated to an engram are reorganized within a narrow time window after a learning episode or over an extended period, potentially mediating continuous functional drift. Optical imaging of *Fos*-inducible transsynaptic markers suggests that coactivated CA3-CA1 PNs preferentially connect with each other at earlier time points after associative learning (*76*). Beyond differences in imaging resolution and data analysis, discrepancies between our findings and prior work may reflect the possibility that non-Hebbian mechanisms, as described here, are preceded by an initial phase of Hebbian plasticity. Further investigation is needed to determine the generalizability of these principles to other circuits. Because MSBs are present in multiple brain regions essential for

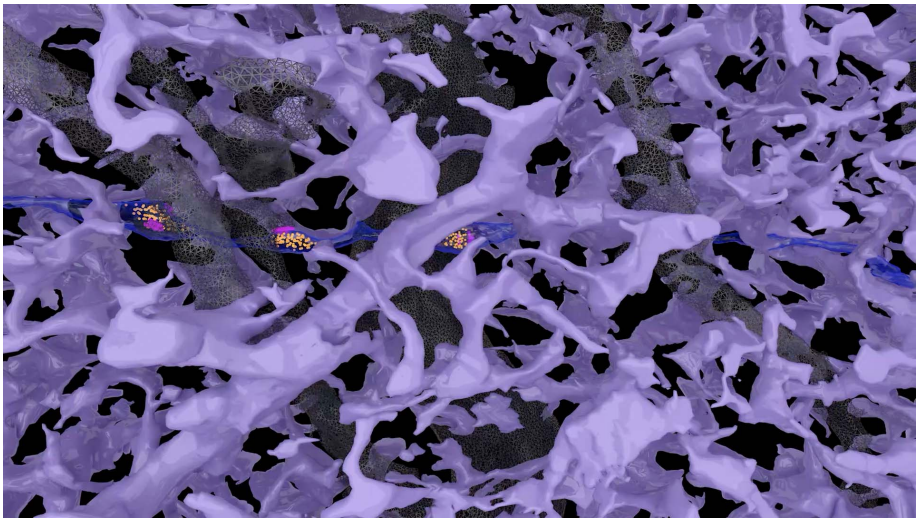

Movie 8. Interfacing of synapses with astrocytes. The animation features a saturated reconstruction of astrocytic processes in the CA1sr. A single SchC axon and its target dendrites are shown as reference points. A zoomed-in 3D view displays astrocytic processes contacting an MSB, with the ATI highlighted. Structures are color coded as indicated in the captions and Fig. 7, A and B.

learning and memory (*51*, *52*, *55*, *56*), it is plausible that their networks undergo progressive remodeling as more information is acquired over the lifespan, and that MSB dysfunctions contribute to cognitive decline. Moreover, the abundance and complexity of these atypical synapses may correlate with general intelligence both across and within mammalian species (*29*).

The mammalian brain comprises numerous neuron subtypes with unique morphologies, synaptic target specificities, and electrophysiological properties (*77*–*81*). It seems unlikely that our findings merely reflect intrinsic features of hippocampal PNs, because the structural hallmarks of long-term memory were undetectable in PNs activated by CS alone. Additionally, dynamic shifts in the excitability and activity-dependent redistribution of the SA have been described, although much of the evidence for the latter is based on artificial neuronal silencing or stimulation (*44*, *58*, *82*–*84*). However, the role of neuronal diversity in engram formation is still poorly understood. For example, associative learning may involve distinct subpopulations of CA3 and CA1 PNs distributed across the radial and dorsoventral axes (*85*, *86*). Furthermore, the encoding of fear memory may be accompanied by different structural changes in the dorsal and ventral CA1, because the latter exhibits greater connectivity with the amygdala (*87*).

Fos-based expression systems are widely used for genetic access to transiently activated neurons in animal models (*2*, *88*). Because *Fos* is induced by patterned excitation, lower but still relevant activity might be missed. Therefore, in this study, we define "activity" as "activity above the threshold for *Fos* induction." The potential limitations of our strategy are mitigated by the specificity and magnitude of the documented effects, which would otherwise be obscured by noise if substantial numbers of relevant neurons and synapses were omitted due to labeling bias.

Lastly, our study does not fully elucidate the functional role of MSBs, and their molecular composition is still unknown. The morphogenesis of MSBs and their interactions with postsynaptic partners are likely regulated by unique repertoires of surface adhesion, scaffolding, and signaling molecules (*89*). Identifying these molecules will require developing new methodologies to access structurally distinct synapse subpopulations with shared cellular origins and neurotransmitter identities. Ultimately, such efforts could facilitate time-lapse imaging and targeted manipulation of MSBs in vivo, advancing our understanding of the core principles of information processing in the brain and potentially leading to new therapeutic strategies to prevent memory loss.

Methods summary

Full details of the materials and methods are presented in the supplementary materials. Briefly, all experiments were conducted in accordance with institutional animal care and use committee–approved protocols. Transiently activated neurons were permanently labeled with the engineered peroxidase APEX2-mGFP. This EM-compatible reporter was introduced through a Cre recombinase-inducible AAV into the hippocampus of mice expressing destabilized Cre (DD-Cre) under the control of the endogenous *Fos* promoter ($Fos^{DD\text{-}Cre}$). Mice underwent contextual fear conditioning, followed by the acute administration of TMP to stabilize DD-Cre, inducing APEX2-mGFP expression in neurons with activity that was correlated with learning. A similar protocol was used to label ensembles activated by a neutral CS. All optical imaging, electrophysiological, and 3D-EM analyses were conducted 7 days later. 3D-EM image stacks were acquired from the dorsal CA1sr using SBEM on a Zeiss Merlin microscope equipped with a Gatan 3View. Subcellular structures were segmented with machine-learning-based platforms CDeep3M and PyTorch Connectomics using convolutional neural networks. 3D reconstructions of local connectomes, single synapses, intracellular membrane organelles, and astrocytes were performed using IMOD, PyIMOD, and VAST. Datasets were categorized based on the activity history of projection neurons by tracing peroxidase staining in axons and dendrites. Numerical values for various structural parameters were extracted using VastTools in MATLAB. Final 3D modeling was performed using the VAST 3D viewer or Blender 3.5. Manual tracing and data extraction were conducted in a "blinded" manner. Quantitative analyses were performed in OriginPro.

REFERENCES AND NOTES

1. A. Holtmaat, K. Svoboda, Experience-dependent structural synaptic plasticity in the mammalian brain. *Nat. Rev. Neurosci.* **10**, 647–658 (2009). doi: 10.1038/nrn2699; pmid: 19693029
2. S. A. Josselyn, S. Tonegawa, Memory engrams: Recalling the past and imagining the future. *Science* **367**, eaaw4325 (2020). doi: 10.1126/science.aaw4325; pmid: 31896692
3. K. P. Berry, E. Nedivi, Spine dynamics: Are they all the same? *Neuron* **96**, 43–55 (2017). doi: 10.1016/j.neuron.2017.08.008; pmid: 28957675
4. P. Caroni, F. Donato, D. Muller, Structural plasticity upon learning: Regulation and functions. *Nat. Rev. Neurosci.* **13**, 478–490 (2012). doi: 10.1038/nrn3258; pmid: 22714019
5. J. C. Magee, C. Grienberger, Synaptic plasticity forms and functions. *Annu. Rev. Neurosci.* **43**, 95–117 (2020). doi: 10.1146/annurev-neuro-090919-022842; pmid: 32075520
6. J. Lisman, Glutamatergic synapses are structurally and biochemically complex because of multiple plasticity processes: Long-term potentiation, long-term depression, short-term potentiation and scaling. *Philos. Trans. R. Soc. Lond. B Biol. Sci.* **372**, 20160260 (2017). doi: 10.1098/rstb.2016.0260; pmid: 28093558
7. K. Fox, M. Stryker, Integrating Hebbian and homeostatic plasticity: Introduction. *Philos. Trans. R. Soc. Lond. B Biol. Sci.* **372**, 20160413 (2017). doi: 10.1098/rstb.2016.0413; pmid: 28093560
8. L. G. Reijmers, B. L. Perkins, N. Matsuo, M. Mayford, Localization of a stable neural correlate of associative memory. *Science* **317**, 1230–1233 (2007). doi: 10.1126/science.1143839; pmid: 17761885
9. X. Liu *et al.*, Optogenetic stimulation of a hippocampal engram activates fear memory recall. *Nature* **484**, 381–385 (2012). doi: 10.1038/nature11028; pmid: 22441246
10. T. Kitamura *et al.*, Engrams and circuits crucial for systems consolidation of a memory. *Science* **356**, 73–78 (2017). doi: 10.1126/science.aam6808; pmid: 28386011
11. K. K. Cowansage *et al.*, Direct reactivation of a coherent neocortical memory of context. *Neuron* **84**, 432–441 (2014). doi: 10.1016/j.neuron.2014.09.022; pmid: 25308330
12. D. S. Roy *et al.*, Brain-wide mapping reveals that engrams for a single memory are distributed across multiple brain regions. *Nat. Commun.* **13**, 1799 (2022). doi: 10.1038/s41467-022-29384-4; pmid: 35379803
13. L. N. Driscoll, L. Duncker, C. D. Harvey, Representational drift: Emerging theories for continual learning and experimental future directions. *Curr. Opin. Neurobiol.* **76**, 102609 (2022). doi: 10.1016/j.conb.2022.102609; pmid: 35939861
14. A. Rubin, N. Geva, L. Sheintuch, Y. Ziv, Hippocampal ensemble dynamics timestamp events in long-term memory. *eLife* **4**, e12247 (2015). doi: 10.7554/eLife.12247; pmid: 26682652
15. Y. Ziv *et al.*, Long-term dynamics of CA1 hippocampal place codes. *Nat. Neurosci.* **16**, 264–266 (2013). doi: 10.1038/nn.3329; pmid: 23396101

16. L. N. Driscoll, N. L. Pettit, M. Minderer, S. N. Chettih, C. D. Harvey, Dynamic reorganization of neuronal activity patterns in parietal cortex. *Cell* **170**, 986–999.e16 (2017). doi: 10.1016/j.cell.2017.07.021; pmid: 28823559
17. C. E. Schoonover, S. N. Ohashi, R. Axel, A. J. P. Fink, Representational drift in primary olfactory cortex. *Nature* **594**, 541–546 (2021). doi: 10.1038/s41586-021-03628-7; pmid: 34108681
18. J. S. Lee, J. J. Briguglio, J. D. Cohen, S. Romani, A. K. Lee, The statistical structure of the hippocampal code for space as a function of time, context, and value. *Cell* **183**, 620–635.e22 (2020). doi: 10.1016/j.cell.2020.09.024; pmid: 33035454
19. W. Denk, H. Horstmann, Serial block-face scanning electron microscopy to reconstruct three-dimensional tissue nanostructure. *PLOS Biol.* **2**, e329 (2004). doi: 10.1371/journal.pbio.0020329; pmid: 15514700
20. N. Kasthuri *et al*., Saturated reconstruction of a volume of neocortex. *Cell* **162**, 648–661 (2015). doi: 10.1016/j.cell.2015.06.054; pmid: 26232230
21. J. L. Morgan, D. R. Berger, A. W. Wetzel, J. W. Lichtman, The fuzzy logic of network connectivity in mouse visual thalamus. *Cell* **165**, 192–206 (2016). doi: 10.1016/j.cell.2016.02.033; pmid: 27015312
22. M. Helmstaedter *et al*., Connectomic reconstruction of the inner plexiform layer in the mouse retina. *Nature* **500**, 168–174 (2013). doi: 10.1038/nature12346; pmid: 23925239
23. F. N. Svara, J. Kornfeld, W. Denk, J. H. Bollmann, Volume EM reconstruction of spinal cord reveals wiring specificity in speed-related motor circuits. *Cell Rep.* **23**, 2942–2954 (2018). doi: 10.1016/j.celrep.2018.05.023; pmid: 29874581
24. M. Winding *et al*., The connectome of an insect brain. *Science* **379**, eadd9330 (2023). doi: 10.1126/science.add9330; pmid: 36893230
25. A. Motta *et al*., Dense connectomic reconstruction in layer 4 of the somatosensory cortex. *Science* **366**, eaay3134 (2019). doi: 10.1126/science.aay3134; pmid: 31649140
26. S. J. Cook *et al*., Whole-animal connectomes of both *Caenorhabditis elegans* sexes. *Nature* **571**, 63–71 (2019). doi: 10.1038/s41586-019-1352-7; pmid: 31270481
27. Y. Mishchenko *et al*., Ultrastructural analysis of hippocampal neuropil from the connectomics perspective. *Neuron* **67**, 1009–1020 (2010). doi: 10.1016/j.neuron.2010.08.014; pmid: 20869597
28. N. L. Turner *et al*., Reconstruction of neocortex: Organelles, compartments, cells, circuits, and activity. *Cell* **185**, 1082–1100.e24 (2022). doi: 10.1016/j.cell.2022.01.023; pmid: 35216674
29. A. Shapson-Coe *et al*., A petavoxel fragment of human cerebral cortex reconstructed at nanoscale resolution. *Science* **384**, eadk4858 (2024). doi: 10.1126/science.adk4858; pmid: 38723085
30. T. Nakashiba, J. Z. Young, T. J. McHugh, D. L. Buhl, S. Tonegawa, Transgenic inhibition of synaptic transmission reveals role of CA3 output in hippocampal learning. *Science* **319**, 1260–1264 (2008). doi: 10.1126/science.1151120; pmid: 18218862
31. S. S. Lam *et al*., Directed evolution of APEX2 for electron microscopy and proximity labeling. *Nat. Methods* **12**, 51–54 (2015). doi: 10.1038/nmeth.3179; pmid: 25419960
32. J. D. Martell, T. J. Deerinck, S. S. Lam, M. H. Ellisman, A. Y. Ting, Electron microscopy using the genetically encoded APEX2 tag in cultured mammalian cells. *Nat. Protoc.* **12**, 1792–1816 (2017). doi: 10.1038/nprot.2017.065; pmid: 28796234
33. B. Dillingham *et al*., Fear learning induces long-lasting changes in gene expression and pathway specific presynaptic growth. *BioRxiv.*, (2019).
34. R. Sando 3rd *et al*., Inducible control of gene expression with destabilized Cre. *Nat. Methods* **10**, 1085–1088 (2013). doi: 10.1038/nmeth.2640; pmid: 24056874
35. V. M. A. Carvalho *et al*., Representation of olfactory information in organized active neural ensembles in the hypothalamus. *Cell Rep.* **32**, 108061 (2020). doi: 10.1016/j.celrep.2020.108061; pmid: 32846119
36. E. L. Yap, M. E. Greenberg, Activity-regulated transcription: Bridging the gap between neural activity and behavior. *Neuron* **100**, 330–348 (2018). doi: 10.1016/j.neuron.2018.10.013; pmid: 30359600
37. M. Iwamoto, T. Björklund, C. Lundberg, D. Kirik, T. J. Wandless, A general chemical method to regulate protein stability in the mammalian central nervous system. *Chem. Biol.* **17**, 981–988 (2010). doi: 10.1016/j.chembiol.2010.07.009; pmid: 20851347
38. C. J. Guenthner, K. Miyamichi, H. H. Yang, H. C. Heller, L. Luo, Permanent genetic access to transiently active neurons via TRAP: Targeted recombination in active populations. *Neuron* **78**, 773–784 (2013). doi: 10.1016/j.neuron.2013.03.025; pmid: 23764283
39. L. Ye *et al*., Wiring and molecular features of prefrontal ensembles representing distinct experiences. *Cell* **165**, 1776–1788 (2016). doi: 10.1016/j.cell.2016.05.010; pmid: 27238022
40. S. Tonegawa, M. D. Morrissey, T. Kitamura, The role of engram cells in the systems consolidation of memory. *Nat. Rev. Neurosci.* **19**, 485–498 (2018). doi: 10.1038/s41583-018-0031-2; pmid: 29970909
41. J. R. Kremer, D. N. Mastronarde, J. R. McIntosh, Computer visualization of three-dimensional image data using IMOD. *J. Struct. Biol.* **116**, 71–76 (1996). doi: 10.1006/jsbi.1996.0013; pmid: 8742726
42. Z. Lin, D. Wei, J. Lichtman, H. Pfister, PyTorch connectomics: A scalable and flexible segmentation framework for em connectomics. arXiv:2112.05754 [eess.IV] (2021).
43. M. G. Haberl *et al*., CDeep3M-Plug-and-Play cloud-based deep learning for image segmentation. *Nat. Methods* **15**, 677–680 (2018). doi: 10.1038/s41592-018-0106-z; pmid: 30171236
44. Y. Zhu *et al*., Nanoscale 3D EM reconstructions reveal intrinsic mechanisms of structural diversity of chemical synapses. *Cell Rep.* **35**, 108953 (2021). doi: 10.1016/j.celrep.2021.108953; pmid: 33826888
45. G. Buzsáki, K. Mizuseki, The log-dynamic brain: How skewed distributions affect network operations. *Nat. Rev. Neurosci.* **15**, 264–278 (2014). doi: 10.1038/nrn3687; pmid: 24569488
46. T. M. Bartol Jr *et al*., Nanoconnectomic upper bound on the variability of synaptic plasticity. *eLife* **4**, e10778 (2015). doi: 10.7554/eLife.10778; pmid: 26618907
47. V. A. Alvarez, B. L. Sabatini, Anatomical and physiological plasticity of dendritic spines. *Annu. Rev. Neurosci.* **30**, 79–97 (2007). doi: 10.1146/annurev.neuro.30.051606.094222; pmid: 17280523
48. A. Attardo, J. E. Fitzgerald, M. J. Schnitzer, Impermanence of dendritic spines in live adult CA1 hippocampus. *Nature* **523**, 592–596 (2015). doi: 10.1038/nature14467; pmid: 26098371
49. F. J. Hwang *et al*., Motor learning selectively strengthens cortical and striatal synapses of motor engram neurons. *Neuron* **110**, 2790–2801.e5 (2022). doi: 10.1016/j.neuron.2022.06.006; pmid: 35809573
50. K. E. Sorra, K. M. Harris, Occurrence and three-dimensional structure of multiple synapses between individual radiatum axons and their target pyramidal cells in hippocampal area CA1. *J. Neurosci.* **13**, 3736–3748 (1993). doi: 10.1523/JNEUROSCI.13-09-03736.1993; pmid: 8366344
51. M. Rigby *et al*., Multi-synaptic boutons are a feature of CA1 hippocampal connections in the stratum oriens. *Cell Rep.* **42**, 112397 (2023). doi: 10.1016/j.celrep.2023.112397; pmid: 37074915
52. E. B. Bloss *et al*., Single excitatory axons form clustered synapses onto CA1 pyramidal cell dendrites. *Nat. Neurosci.* **21**, 353–363 (2018). doi: 10.1038/s41593-018-0084-6; pmid: 29459763
53. N. Toni, P. A. Buchs, I. Nikonenko, C. R. Bron, D. Muller, LTP promotes formation of multiple spine synapses between a single axon terminal and a dendrite. *Nature* **402**, 421–425 (1999). doi: 10.1038/46574; pmid: 10586883
54. Y. Geinisman, R. W. Berry, J. F. Disterhoft, J. M. Power, E. A. Van der Zee, Associative learning elicits the formation of multiple-synapse boutons. *J. Neurosci.* **21**, 5568–5573 (2001). doi: 10.1523/JNEUROSCI.21-15-05568.2001; pmid: 11466428
55. N. G. Hedrick *et al*., Learning binds new inputs into functional synaptic clusters via spinogenesis. *Nat. Neurosci.* **25**, 726–737 (2022). doi: 10.1038/s41593-022-01086-6; pmid: 35654957
56. Y. Yang *et al*., Selective synaptic remodeling of amygdalocortical connections associated with fear memory. *Nat. Neurosci.* **19**, 1348–1355 (2016). doi: 10.1038/nn.4370; pmid: 27595384
57. J. Liu *et al*., Fear memory-associated synaptic and mitochondrial changes revealed by deep learning-based processing of electron microscopy data. *Cell Rep.* **40**, 111151 (2022). doi: 10.1016/j.celrep.2022.111151; pmid: 35926462
58. K. M. Harris, Structural LTP: From synaptogenesis to regulated synapse enlargement and clustering. *Curr. Opin. Neurobiol.* **63**, 189–197 (2020). doi: 10.1016/j.conb.2020.04.009; pmid: 32659458
59. Y. Hirabayashi *et al*., ER-mitochondria tethering by PDZD8 regulates Ca^{2+} dynamics in mammalian neurons. *Science* **358**, 623–630 (2017). doi: 10.1126/science.aan6009; pmid: 29097544
60. S. K. Kwon *et al*., LKB1 regulates mitochondria-dependent presynaptic calcium clearance and neurotransmitter release properties at excitatory synapses along cortical axons. *PLOS Biol.* **14**, e1002516 (2016). doi: 10.1371/journal.pbio.1002516; pmid: 27429220
61. M. J. Devine, J. T. Kittler, Mitochondria at the neuronal presynapse in health and disease. *Nat. Rev. Neurosci.* **19**, 63–80 (2018). doi: 10.1038/nrn.2017.170; pmid: 29348666
62. M. Bell, T. Bartol, T. Sejnowski, P. Rangamani, Dendritic spine geometry and spine apparatus organization govern the spatiotemporal dynamics of calcium. *J. Gen. Physiol.* **151**, 1017–1034 (2019). doi: 10.1085/jgp.201812261; pmid: 31324651
63. A. Konietzny, S. Wegmann, M. Mikhaylova, The endoplasmic reticulum puts a new spin on synaptic tagging. *Trends Neurosci.* **46**, 32–44 (2023). doi: 10.1016/j.tins.2022.10.012; pmid: 36428191
64. H. L. Smith *et al*., Mitochondrial support of persistent presynaptic vesicle mobilization with age-dependent synaptic growth after LTP. *eLife* **5**, e15275 (2016). doi: 10.7554/eLife.15275; pmid: 27991850
65. A. Maximov, T. C. Südhof, Autonomous function of synaptotagmin 1 in triggering synchronous release independent of asynchronous release. *Neuron* **48**, 547–554 (2005). doi: 10.1016/j.neuron.2005.09.006; pmid: 16301172
66. T. L. Lewis Jr., S. K. Kwon, A. Lee, R. Shaw, F. Polleux, MFF-dependent mitochondrial fission regulates presynaptic release and axon branching by limiting axonal mitochondria size. *Nat. Commun.* **9**, 5008 (2018). doi: 10.1038/s41467-018-07416-2; pmid: 30479337
67. N. J. Allen, C. Eroglu, Cell biology of astrocyte-synapse interactions. *Neuron* **96**, 697–708 (2017). doi: 10.1016/j.neuron.2017.09.056; pmid: 29096081
68. B. S. Khakh, M. V. Sofroniew, Diversity of astrocyte functions and phenotypes in neural circuits. *Nat. Neurosci.* **18**, 942–952 (2015). doi: 10.1038/nn.4043; pmid: 26108722
69. A. Kol *et al*., Astrocytes contribute to remote memory formation by modulating hippocampal-cortical communication during learning. *Nat. Neurosci.* **23**, 1229–1239 (2020). doi: 10.1038/s41593-020-0679-6; pmid: 32747787
70. W. Sun *et al*., Spatial transcriptomics reveal neuron-astrocyte synergy in long-term memory. *Nature* **627**, 374–381 (2024). doi: 10.1038/s41586-023-07011-6; pmid: 38326616
71. M. B. Chen, X. Jiang, S. R. Quake, T. C. Südhof, Persistent transcriptional programmes are associated with remote memory. *Nature* **587**, 437–442 (2020). doi: 10.1038/s41586-020-2905-5; pmid: 33177708
72. A. Maximov, O. H. Shin, X. Liu, T. C. Südhof, Synaptotagmin-12, a synaptic vesicle phosphoprotein that modulates spontaneous neurotransmitter release. *J. Cell Biol.* **176**, 113–124 (2007). doi: 10.1083/jcb.200607021; pmid: 17190793
73. R. L. Redondo, R. G. Morris, Making memories last: The synaptic tagging and capture hypothesis. *Nat. Rev. Neurosci.* **12**, 17–30 (2011). doi: 10.1038/nrn2963; pmid: 21170072
74. T. Rogerson *et al*., Synaptic tagging during memory allocation. *Nat. Rev. Neurosci.* **15**, 157–169 (2014). doi: 10.1038/nrn3667; pmid: 24496410
75. N. Matsuo, L. Reijmers, M. Mayford, Spine-type-specific recruitment of newly synthesized AMPA receptors with learning. *Science* **319**, 1104–1107 (2008). doi: 10.1126/science.1149967; pmid: 18292343
76. J. H. Choi *et al*., Interregional synaptic maps among engram cells underlie memory formation. *Science* **360**, 430–435 (2018). doi: 10.1126/science.aas9204; pmid: 29700265
77. B. Wamsley, G. Fishell, Genetic and activity-dependent mechanisms underlying interneuron diversity. *Nat. Rev. Neurosci.* **18**, 299–309 (2017). doi: 10.1038/nrn.2017.30; pmid: 28381833
78. D. L. Hunt, D. Linaro, B. Si, S. Romani, N. Spruston, A novel pyramidal cell type promotes sharp-wave synchronization in the hippocampus. *Nat. Neurosci.* **21**, 985–995 (2018). doi: 10.1038/s41593-018-0172-7; pmid: 29915194
79. Z. Yao *et al*., A high-resolution transcriptomic and spatial atlas of cell types in the whole mouse brain. *Nature* **624**, 317–332 (2023). doi: 10.1038/s41586-023-06812-z; pmid: 38092916
80. M. Zhang *et al*., Molecularly defined and spatially resolved cell atlas of the whole mouse brain. *Nature* **624**, 343–354 (2023). doi: 10.1038/s41586-023-06808-9; pmid: 38092912
81. Z. Yao *et al*., A taxonomy of transcriptomic cell types across the isocortex and hippocampal formation. *Cell* **184**,

3222–3241.e26 (2021). doi: 10.1016/j.cell.2021.04.021; pmid: 34004146
82. D. J. Cai *et al*., A shared neural ensemble links distinct contextual memories encoded close in time. *Nature* **534**, 115–118 (2016). doi: 10.1038/nature17955; pmid: 27251287
83. M. Pignatelli *et al*., Engram Cell Excitability State Determines the Efficacy of Memory Retrieval. *Neuron* **101**, 274–284.e5 (2019). doi: 10.1016/j.neuron.2018.11.029; pmid: 30551997
84. A. J. Mocle *et al*., Excitability mediates allocation of pre-configured ensembles to a hippocampal engram supporting contextual conditioned threat in mice. *Neuron* **112**, 1487–1497.e6 (2024). doi: 10.1016/j.neuron.2024.02.007; pmid: 38447576
85. I. Soltesz, A. Losonczy, CA1 pyramidal cell diversity enabling parallel information processing in the hippocampus. *Nat. Neurosci.* **21**, 484–493 (2018). doi: 10.1038/s41593-018-0118-0; pmid: 29593317
86. M. S. Cembrowski, N. Spruston, Heterogeneity within classical cell types is the rule: Lessons from hippocampal pyramidal neurons. *Nat. Rev. Neurosci.* **20**, 193–204 (2019). doi: 10.1038/s41583-019-0125-5; pmid: 30778192
87. J. C. Jimenez *et al*., Contextual fear memory retrieval by correlated ensembles of ventral CA1 neurons. *Nat. Commun.* **11**, 3492 (2020). doi: 10.1038/s41467-020-17270-w; pmid: 32661319
88. L. Luo, E. M. Callaway, K. Svoboda, Genetic dissection of neural circuits: A decade of progress. *Neuron* **98**, 865 (2018). doi: 10.1016/j.neuron.2018.05.004; pmid: 29772206
89. T. C. Südhof, Towards an understanding of synapse formation. *Neuron* **100**, 276–293 (2018). doi: 10.1016/j.neuron.2018.09.040; pmid: 30359597

ACKNOWLEDGMENTS

We thank A. Patapoutian, M. Scanziani, H. Cline, and the members of the Maximov and Ellisman laboratories for advice and critical comments. During the preparation of this work, the corresponding author used ChatGPT-4o to assist with proofreading the main text. No generative AI tools were used to produce new content. The authors take full responsibility for the content of this publication. **Funding:** This study was supported by the US National Institutes of Health (grants R01MH118442, R01NS087026, and RF1 MH123224 to A.M.). **Author contributions:** Conceptualization: M.U., Yo.Z., M.E., A.M.; Investigation: M.U., Yo.Z., K.C., F.S.P., E.Z., D.L., L.C., D.Y., T.C.M., M.K., Yut.Z., G.W., T.Q., L.P., A.S., Yux.Z., E.Beu., W.Z., B.D., A.K., A.G., E.M., A.M.; Methodology: M.U., Yo.Z., E.Bus., M.H., K.Y.K., G.W., Yux.Z., L.S.; Visualization: M.U., K.C., E.Z., W.Z.; Supervision: M.E., A.M.; Writing – original draft: A.M.; Writing – review & editing: A.M., M.E., M.U., K.C., E.Z., G.W. **Competing interests:** The authors declare no competing interests. **Data and materials availability:** All numerical values needed to evaluate the conclusions of the paper are provided in the supplementary materials. All other reagents and resources can be obtained from AM upon request. The original SBEM datasets are publicly available at the Cell Image Library (https://doi.org/10.7295/W9P20506).

SUPPLEMENTARY MATERIALS

science.org/doi/10.1126/science.ado8316
Materials and Methods
Figs. S1 to S14
References (*90*–*99*)
MDAR Reproducibility Checklist
Data S1 to S5

Submitted 22 February 2024; accepted 17 December 2024
10.1126/science.ado8316

Synaptic architecture of a memory engram in the mouse hippocampus

Marco Uytiepo, Yongchuan Zhu, Eric Bushong, Katherine Chou, Filip Souza Polli, Elise Zhao, Keun-Young Kim, Danielle Luu, Lyanne Chang, Dong Yang, Tsz Ching Ma, Mingi Kim, Yuting Zhang, Grant Walton, Tom Quach, Matthias Haberl, Luca Patapoutian, Arya Shahbazi, Yuxuan Zhang, Elizabeth Beutter, Weiheng Zhang, Brian Dong, Aureliano Khoury, Alton Gu, Elle McCue, Lisa Stowers, Mark Ellisman, and Anton Maximov

Science **387** (6740), eado8316. DOI: 10.1126/science.ado8316

Editor's summary

How are memories formed and stored in the brain? Uytiepo *et al*. used three-dimensional electron microscopy coupled with chemogenetic tagging and behavioral analysis to determine the structural changes supporting the acquisition of long-term fear memories, focusing on the Schaffer collateral synapses. Long-term memory acquisition was found to be associated with a selective increase in multisynaptic boutons without the involvement of simultaneous activation of synaptically connected neurons. These results challenge the general applicability of the Hebbian model and expand our understanding of the mechanisms responsible for memory formation. —Mattia Maroso